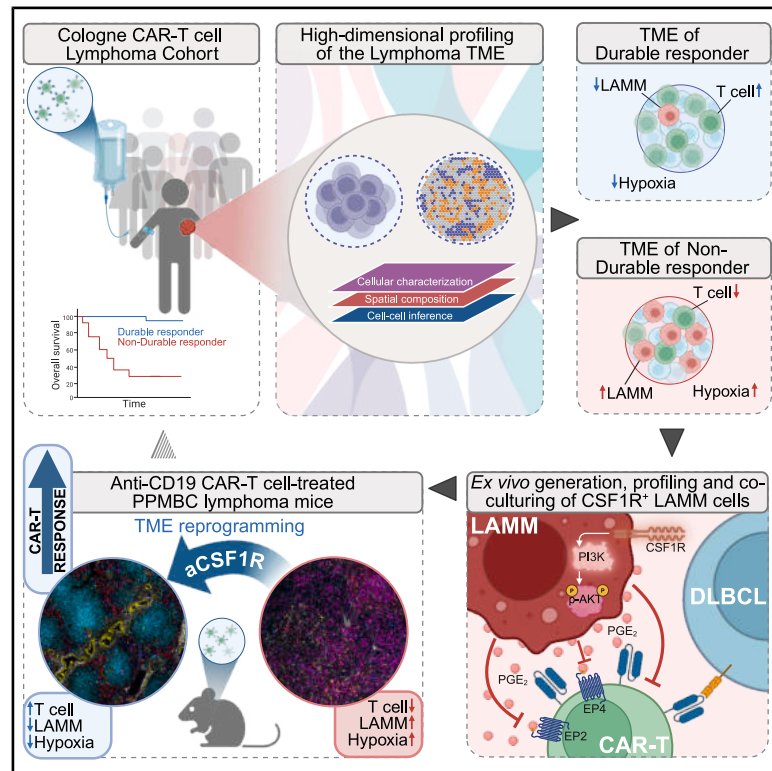


Cancer Cell

CSF1R⁺ myeloid-monocytic cells drive CAR-T cell resistance in aggressive B cell lymphoma

Graphical abstract



Authors

David Stahl, Philipp Gödel, Hyatt Balke-Want, ..., Nima Abedpour, Peter Borchmann, Roland T. Ullrich

Correspondence

roland.ullrich@uk-koeln.de

In brief

Stahl et al. identify a CSF1R⁺ myeloid-monocytic population in primary human B-NHL that suppresses CAR-T cell activity both *in vitro* and *in vivo*. Combining CAR-T cells with CSF1R blockade reprograms the lymphoma tumor microenvironment (TME) and enhances treatment efficacy in an autochthonous mouse model. These findings warrant further clinical investigation.

Highlights

- CSF1R⁺CD14⁺CD68⁺ LAMM cells predict poor response to CAR-T cell therapy in B-NHL
- CSF1R-AKT signaling drives LAMM cell development
- CSF1R⁺ LAMM cells inhibit CAR-T cell function via PGE₂-EP2/4 axis
- CSF1R inhibition reprograms the TME and enhances response to CAR-T cells *in vivo*

Article

CSF1R⁺ myeloid-monocytic cells drive CAR-T cell resistance in aggressive B cell lymphoma

David Stahl,^{1,2,3,4,5,33} Philipp Gödel,^{1,2,4,33} Hyatt Balke-Want,^{1,2,4,6,33} Rahil Gholamipoorfarid,^{1,7} Paul Segbers,^{1,2,5} Luis Tetenborg,^{1,2,5} Mirjam Koker,^{1,2} Janina Dörr,⁸ Lisa Gregor,⁸ Daniel Bachurski,^{1,2,5,9} France Rose,^{2,10} Adrian G. Simon,¹¹ Zinaida Good,^{6,12,13} Josefine Jakob,^{14,15} Björn Häupl,^{14,15,16,17} Marieke Nill,^{1,2} Ruth Flümman,^{1,4,5,18} Tobias Riet,^{1,2} Dinah Lange,^{2,19,20} Stuart J. Blakemore,^{1,21} Herrad Baumann,²² Conrad-Amadeus Voltin,²³ Nicole Potter,²⁴ Lilli Schlözer,^{1,2,5} Max Freihammer,¹ Svenja Wagener-Ryczek,¹¹ Andra-Iza Iuga,²⁵ Jan-Michel Heger,^{1,3,4,5} Hanna Ludwig,^{1,2,4} Julia K. Schleifenbaum,^{1,4} Jessica Propp,^{1,2,4} Paul J. Bröckelmann,^{1,4,5,18}

(Author list continued on next page)

¹Department I of Internal Medicine, Center for Integrated Oncology Aachen Bonn Cologne Duesseldorf, University of Cologne, Faculty of Medicine and University Hospital Cologne, Cologne, Germany

²Center for Molecular Medicine Cologne (CMMC), University of Cologne, Cologne, Germany

³Eise Kröner Forschungskolleg Clonal Evolution in Cancer, University Hospital Cologne, Cologne, Germany

⁴Cancer Research Center Cologne Essen (CCCE), Faculty of Medicine and University Hospital Cologne, University of Cologne, Cologne, Germany

⁵Mildred Scheel School of Oncology Aachen Bonn Cologne Düsseldorf (MSSO ABCD), Faculty of Medicine and University Hospital of Cologne, Cologne, Germany

⁶Stanford Center for Cancer Cell Therapy, Stanford Cancer Institute, Stanford University, Stanford, CA, USA

⁷Department of Translational Genomics, Faculty of Medicine and University Hospital Cologne, University of Cologne, Cologne, Germany

⁸Division of Clinical Pharmacology, Department of Medicine IV, LMU University Hospital, Member of the German Center for Lung Research (DZL), LMU Munich, Munich, Germany

⁹CECAD Center of Excellence on Cellular Stress Responses in Aging-Associated Diseases, University of Cologne, Cologne, Germany

¹⁰University of Cologne, Institute for Biomedical Informatics, Faculty of Medicine and University Hospital Cologne, Cologne, Germany

¹¹Institute of Pathology, University Hospital Cologne, Faculty of Medicine, University of Cologne, Cologne, Germany

¹²Department of Biomedical Data Science, Stanford University School of Medicine, Stanford, CA, USA

¹³Parker Institute for Cancer Immunotherapy, Stanford University School of Medicine, Stanford, CA, USA

¹⁴Department of Medicine, Hematology and Oncology, University Hospital, Goethe University Frankfurt, Frankfurt am Main, Germany

(Affiliations continued on next page)

SUMMARY

Despite the improvement, approximately 60% of patients with relapsed or refractory (*r/r*) aggressive B cell lymphoma (B-NHL) do not achieve durable benefit from CAR-T cell therapy. To elucidate factors associated with CAR-T therapy resistance, we conducted high-dimensional analyses of pre- and post-CAR-T cell specimens. In patients with non-durable response, we identified a prognostically relevant lymphoma-associated myeloid-monocytic (LAMM) gene signature. In-depth profiling revealed a distinct CSF1R⁺CD14⁺CD68⁺ LAMM cell population in both human and murine B-NHL that inhibits CAR-T cell function and correlates with poor outcome. Cell-cell inference analysis uncovered that LAMM cells impair CAR-T cell function through a direct LAMM-T cell interaction via the PGE₂-EP2/EP4 axis. In an autochthonous lymphoma mouse model, combined anti-CD19 CAR-T cell therapy with CSF1R blockade exhibited synergistic effects and improved survival. These findings provide strong rationale for combining anti-CD19 CAR-T cells with CSF1R inhibitors in treating *r/r* aggressive B-NHL patients.

INTRODUCTION

Chimeric antigen receptor T (CAR-T) cell therapy has revolutionized treatment of patients with relapsed or refractory (*r/r*) aggressive B-NHL. CD19-directed CAR-T cells have demonstrated potent activity, leading to approvals in a variety of aggressive B-NHL.^{1,2} However, up to two-thirds of anti-CD19 CAR-T cell-

treated aggressive B-NHL patients do not show long-term benefit and oftentimes succumb to their disease.^{3,4} To date, molecular and cellular mechanisms that underlie CAR-T cell failure and, ultimately, resistance have been attributed to antigen downregulation⁵ or mutation,^{6,7} expansion of regulatory CAR-T (CAR-T_{reg}) cells,^{8,9} and a suppressive lymphoma tumor microenvironment (TME).¹⁰ To overcome these mechanisms of CAR-T

Ron D. Jachimowicz,^{1,4,9,18} Gero Knittel,^{4,26} Sven Borchmann,¹ Sabine Merkelbach-Bruse,¹¹ Christian Pallasch,^{1,4,21} Martin Peifer,^{2,7} Jan Rybniker,^{2,19,20} Alexander Quaas,¹¹ Mark Nitz,²⁴ Johannes Brägelmann,^{2,5,7} Werner Müller,²² Thorsten Persigehl,²⁵ Katarzyna Bozek,^{2,9,10} Sebastian J. Theobald,^{2,19,20} Reinhard Büttner,^{11,27} Thomas Oellerich,^{14,15,16,17,28} Michael Hallek,^{1,2,4,9,27} Sebastian Kobold,^{8,29,30} Markus Chmielewski,^{1,2} Hans Christian Reinhardt,^{4,26,27} Crystal Mackall,^{6,13,31,32} Nima Abedpour,^{1,4,7} Peter Borchmann,^{1,4} and Roland T. Ullrich^{1,2,4,27,34,*}

¹⁵Frankfurt Cancer Institute (FCI), Frankfurt am Main, Germany

¹⁶German Cancer Consortium (DKTK), partner site Frankfurt/Mainz, a partnership between DKFZ and UCT Frankfurt-Marburg, Germany, Frankfurt am Main, Germany

¹⁷German Cancer Research Center (DKFZ), Heidelberg, Germany

¹⁸Max Planck Institute for Biology of Ageing, Cologne, Germany

¹⁹Department I of Internal Medicine, Division of Infectious Diseases, Medical Faculty and University Hospital Cologne, University of Cologne, Cologne, Germany

²⁰German Center for Infection Research (DZIF), Bonn-Cologne, Germany

²¹Department I of Internal Medicine, Translational Research for Infectious Diseases and Oncology (TRIO), University Hospital Clinic of Cologne, Cologne, Germany

²²Miltenyi Biotec B.V. & Co. KG, Bergisch Gladbach, Germany

²³Department of Nuclear Medicine, Faculty of Medicine and University Hospital Cologne, University of Cologne, Cologne, Germany

²⁴Department of Chemistry, University of Toronto, Toronto, ON M5S 3H6, Canada

²⁵Institute for Diagnostic and Interventional Radiology, Faculty of Medicine and University Hospital Cologne, University Cologne, Cologne, Germany

²⁶Department of Hematology and Stem Cell Transplantation, West German Cancer Center, German Cancer Consortium Partner Site Essen, Center for Molecular Biotechnology, University Hospital Essen, University of Duisburg-Essen, Essen, Germany

²⁷National Center for Tumor Diseases (NCT), NCT West, Cologne, Germany

²⁸University Cancer Center (UCT), Frankfurt am Main, Germany

²⁹German Cancer Consortium (DKTK), Partner Site Munich, a partnership between the DKFZ Heidelberg and the University Hospital of the LMU, Munich, Germany

³⁰Einheit für Klinische Pharmakologie (EKLiP), Helmholtz Zentrum München – German Research Center for Environmental Health Neuherberg, Munich, Germany

³¹Department of Pediatrics, Stanford University, Stanford, CA, USA

³²Department of Medicine, Stanford University, Stanford, CA, USA

³³These authors contributed equally

³⁴Lead contact

*Correspondence: roland.ullrich@uk-koeln.de

<https://doi.org/10.1016/j.ccell.2025.05.013>

cell failure, for instance, antigen downregulation can be addressed by utilizing multi-targeted CAR-T cells¹¹ and CAR-T_{reg} cells can be depleted from manufactured products, e.g., via CD25 selection.⁸ Correlative transcriptomic studies involving samples from CAR-T cell-treated aggressive B-NHL patients indicate a relevant role of the TME in response and resistance to CAR-T cell therapy.^{10,12,13} However, targeting the TME in aggressive B-NHL to boost efficacy of CAR-T cells has not yet been sufficiently explored.

It is established that under pathological conditions such as chronic inflammation or cancer, bone marrow and spleen show an enhanced output of immature myeloid cells. These cells accumulate and fail to fully differentiate into functional macrophages, dendritic cells, or neutrophils. Instead, they exert immunosuppressive functions e.g., via interleukin 10 (IL-10), transforming growth factor β 1 (TGF- β 1), and prostaglandin E2 (PGE₂) with T cell inhibition being the most relevant for their functional taxonomy.^{14,15} In an attempt to provide a classification summarizing the origin, function, and spectrum of these cells, they were initially termed myeloid-derived suppressor cells (MDSCs),¹⁶ and later grouped into polymorphonuclear (PMN)- and monocytic (M)-MDSCs.^{17,18} In tumors, M-MDSCs deviate from intermediate states of monocytes toward tumor-associated macrophages (TAMs), which is driven by hypoxia and activation of the hypoxia-inducible factor 1 α

(HIF1 α).¹⁸ Differentiation of M-MDSCs toward TAMs is characterized by downregulation of CD14 and upregulation of CD68 as well as colony stimulating factor 1 receptor (CSF1R). Here, the receptor tyrosine kinase CSF1R takes center stage by promoting expansion and the developmental shift toward TAMs.¹⁹ At the molecular level, the PI3K/AKT/mTOR axis has been identified as a key downstream target.²⁰ While extensive work has been conducted to characterize prognostically relevant features of the TME in aggressive B-NHL, especially within the context of CAR-T cell therapy,^{10,12,13} our knowledge on the functional interplay of the myeloid cell compartment with other cell populations, including CAR-T cells, is scarce and warrants further investigation to develop therapeutic strategies for reprogramming the TME and thereby overcome resistance against CAR-T cell therapy in aggressive B-NHL.²¹

We herein aimed to elaborate mechanisms that are associated with CAR-T cell treatment failure and performed high-dimensional analyses using bulk RNA sequencing (bulk RNA-seq), single-cell RNA sequencing (scRNA-seq), imaging mass cytometry (IMC), and MACSima imaging cyclic staining (MICS) in durable and non-durable responding CAR-T cell patients with the ultimate goal to identify potential therapeutic targets within the TME to be validated in our CAR-T cell-treated lymphoma mouse model.

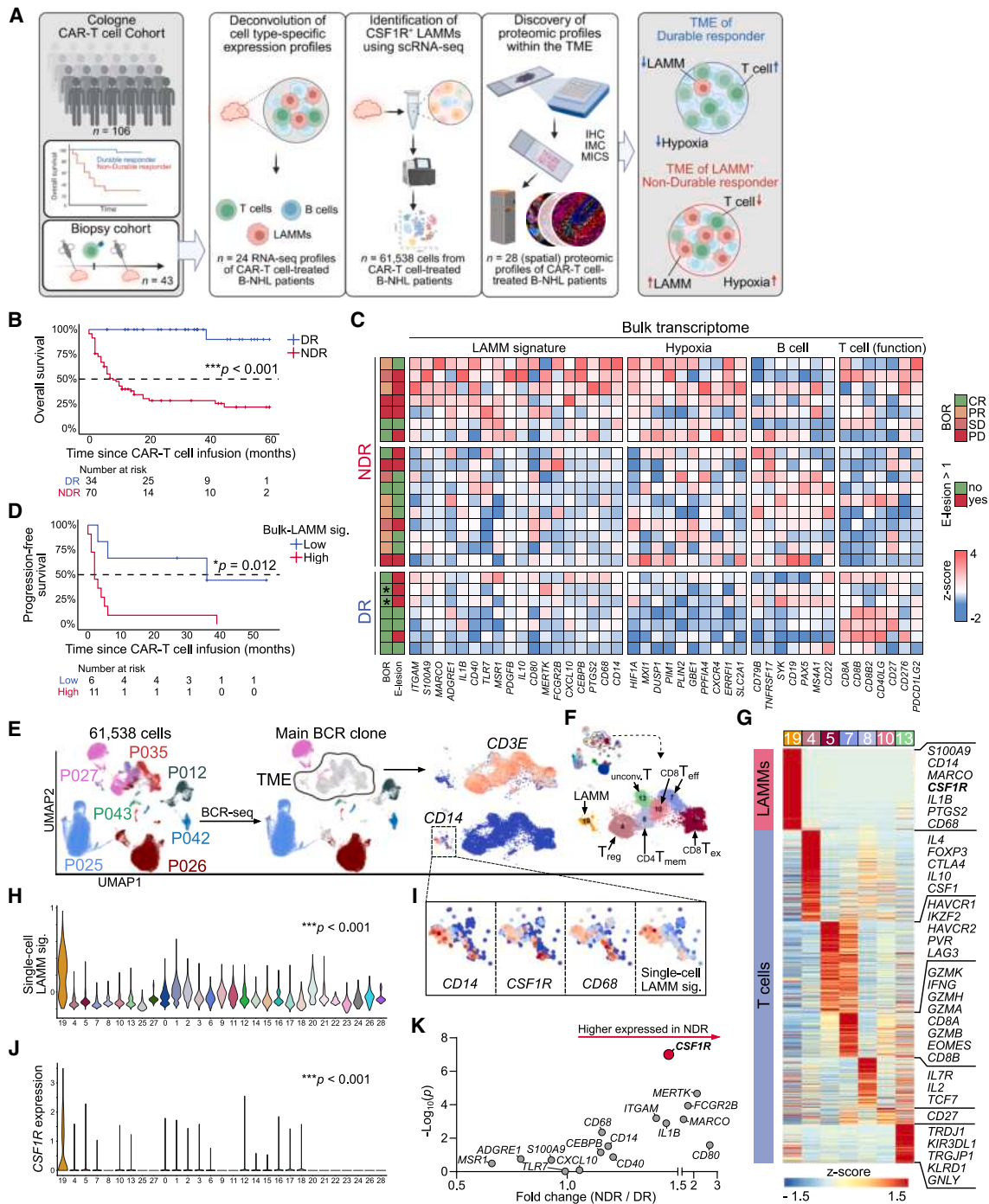


Figure 1. A LAMM cell-derived gene signature is prognostically relevant in CAR-T cell-treated aggressive B-NHL and LAMM cells express CSF1R

(A) Schematic study design.

(B) Overall survival (OS) of the study cohort ($n = 104$, $p < 0.001$, log rank test). Durable responders (DR) defined as complete remission six months after CAR-T cell therapy.

(C) Heatmap of aggressive B-NHL before CAR-T cell therapy ($n = 24$). *DR patient receiving radiation therapy within six months post-CAR-T cell therapy who was excluded from downstream evaluation of clinical data.

(D) Progression-free survival (PFS) of the biopsy cohort ($n = 17$, $p = 0.012$, log rank test).

(E) scRNA-seq of aggressive B-NHL samples before CAR-T cell therapy. Highlighted are single patients, their main B cell receptor (BCR) clone and the overlapping TME.

(F) Phenographic clustering.

(legend continued on next page)

RESULTS

A CSF1R⁺ lymphoma-associated myeloid-monocytic (LAMM) cell population associates with CAR-T cell failure in patients with aggressive B-NHL

To elucidate hallmarks of an immunosuppressive TME resulting in CAR-T cell resistance in patients with aggressive B-NHL, we applied high-dimensional analysis including bulk RNA-seq, scRNA-seq, IMC, and MICS to aggressive B-NHL specimens obtained at baseline and after CAR-T cell infusion (Figure 1A). Our cohort consisted of 106 patients with aggressive B-NHL treated with CAR-T cells at the University Hospital of Cologne (Table S1). Complete remission six months after CAR-T cell therapy, defined as durable response (DR), results in improved patient progression-free (PFS) and overall survival (OS) and correlates with lower metabolic tumor volume (MTV) prior to treatment^{3,22–24} (Figures 1B and S1A–S1C), but not with Cell-of-Origin (COO) (Figures S1D–S1F). We performed bulk RNA-seq (Figures S1G and S1H) and found a strong enrichment of tumor hypoxia, glycolysis, and reactive oxygen species pathways in aggressive B-NHL with non-durable response (NDR) to CAR-T cell treatment (Figures S1I–S1K). In line with the hypoxic TME, we observed an enrichment of myeloid-monocytic associated genes consisting of *CD14*, *ITGAM*, *CD68*, *S100A9*, *CEBPB*, *PTGS2*, *IL10*,¹⁷ *CD80*, *CD40*, *MARCO*, *ADGRE1*, *TLR7*,²⁵ *MSR1*,²⁶ *MERTK*,²⁷ *FCGR2B*,²⁸ *PDGFB*,²⁹ *CXCL10*,³⁰ and *IL1B*³¹ in patients with NDR (Figure 1C). Strikingly, high expression of the immunosuppressive LAMM gene signature was associated with worse outcome (Figures 1D and S1L).

To further characterize a LAMM cell population driving the expression of our LAMM gene signature, we performed scRNA-seq of 61,538 cells derived from seven independent primary human B-NHL specimens before CAR-T cell therapy (Figure S2A). By employing B cell receptor sequencing (BCR-seq), we separated individual aggressive B-NHL-derived malignant B cells from the shared TME across all samples (Figures 1E and S2B). In addition, we identified a population of the shared TME to express *CD14* (Figure 1E). Unbiased phenographic clustering identified a total of 29 clusters (Figure S2C), indicated that the TME consisted of six T cell (C4, C5, C7, C8, C10, and C13) and a single myeloid-monocytic cluster (C19) (Figure 1F) and showed that cells from C19 were present in all patient samples (Figure S2D). To better characterize each TME cluster, we applied differential gene expression analysis and found that C19 is driven by the expression of *CD14*, *CD68*, *IL1B*, *MARCO*, *PTGS2*, and *S100A9* (Figure 1G). Thus, C19 faithfully recapitulates the LAMM cell population at the single-cell level (Figures 1H, 1I, S2E, and S2F). Moreover, our scRNA-seq analysis revealed the expression of *CSF1R* – a well-known key regulator for the differentiation and expansion of immunosuppressive TAMs³² (Figures 1I and 1J). Finally, we analyzed the expression of each

LAMM gene as well as *CSF1R* in our scRNA-seq dataset and observed higher expression levels of *CSF1R*, *CD14*, and *CD68* in patients with NDR (Figure 1K). To corroborate our findings, we correlated the *CSF1R* expression derived from bulk RNA-seq with the LAMM gene signature (Figure S2G). These observations indicate a potential impact of LAMM cells in the TME of aggressive B-NHL treated with CAR-T cells.

Infiltration with LAMM cells associates with T cell exclusion and resistance to CAR-T cell therapy

We next aimed to unravel the impact of LAMM cells on the cellular composition of the TME. To this end, we performed IMC of human aggressive B-NHL specimens prior to CAR-T cell therapy (Figure 1A; Table S2). In line with our scRNA-seq data, we identified CD14⁺CD68⁺ LAMM cells co-expressing *CSF1R* (Figure 2A). CD14⁺CD68⁺ LAMM cells were enriched in NDR samples and associated with lower infiltration of T cells (Figures 2B, S3A, and S3B). Clinical correlation of our IMC dataset allowed to confirm that high infiltration of CD14⁺ and CD68⁺ LAMM cells was associated with shortened PFS after CAR-T cell therapy (Figure 2C). Most strikingly, high LAMM cell infiltration and low CD8⁺ T cell infiltration before undergoing CAR-T cell therapy showed a significantly reduced PFS when compared to aggressive B-NHL with low LAMM and high CD8⁺ T cell infiltration (Figure 2D). Next, we independently confirmed in our transcriptomic dataset that patients with a high LAMM gene signature and NDR showed both a lower total and CD8⁺ T cell fraction using CIBERSORTx,³³ an *in silico* approach which enables to determine the relative cellular composition of immune cells from bulk RNA-seq data (Figures S3C and S3D). Importantly, the combination of a high LAMM gene signature and low CD8⁺ T cell infiltration was associated with worse outcome, as compared to a low LAMM gene signature with high CD8⁺ T cell infiltration within our transcriptomic dataset (Figures S3E and S3F). As part of our biopsy program, we additionally obtained samples shortly after CAR-T cell infusion and at disease progression following CAR-T cell therapy. Here, we found that LAMM cells surrounded CD31⁺ endothelial cells of tumor blood vessels and were in close proximity to CD3⁺ and CD8⁺ cytotoxic T cells, possibly impeding the penetration of T cells into lymphoma tissue (Figures 2E and S3G).

To facilitate clinical implementation and to independently confirm the relevance of *CSF1R* expression in LAMM cells, we next performed immunohistochemistry (IHC) for *CSF1R* (Figures 2F and S3H). Our IHC data confirmed enhanced infiltration of *CSF1R*⁺ LAMM cells in aggressive B-NHL patients with NDR, as compared to patients with DR (Figure 2G). Furthermore, high *CSF1R* H-score was associated with worse survival in CAR-T cell-treated B-NHL patients (Figures 2H and S3I). Nevertheless, for clinical implementation, validation of this finding including the chosen threshold for *CSF1R* positivity in a larger cohort will be necessary.

(G) Heatmap summarizing top 300 most significantly upregulated genes in TME clusters (LAMM cells: C19; T cells: C4, C5, C7, C8, C10, C13).

(H) Single-cell LAMM signature across all phenographic clusters (Kruskal-Wallis test).

(I) Key LAMM genes (*CD14*, *CSF1R*, *CD68*) and LAMM signature expression in C19.

(J) Single-cell *CSF1R* expression across all phenographic clusters (Kruskal-Wallis test).

(K) Dot plot indicating fold change of the mean expression of LAMM signature genes including *CSF1R* at the single-cell level in C19 from patients with NDR versus DR. *p*-values indicate unpaired *t* test (two-tailed). Also see Figures S1, S2, and Table S1.

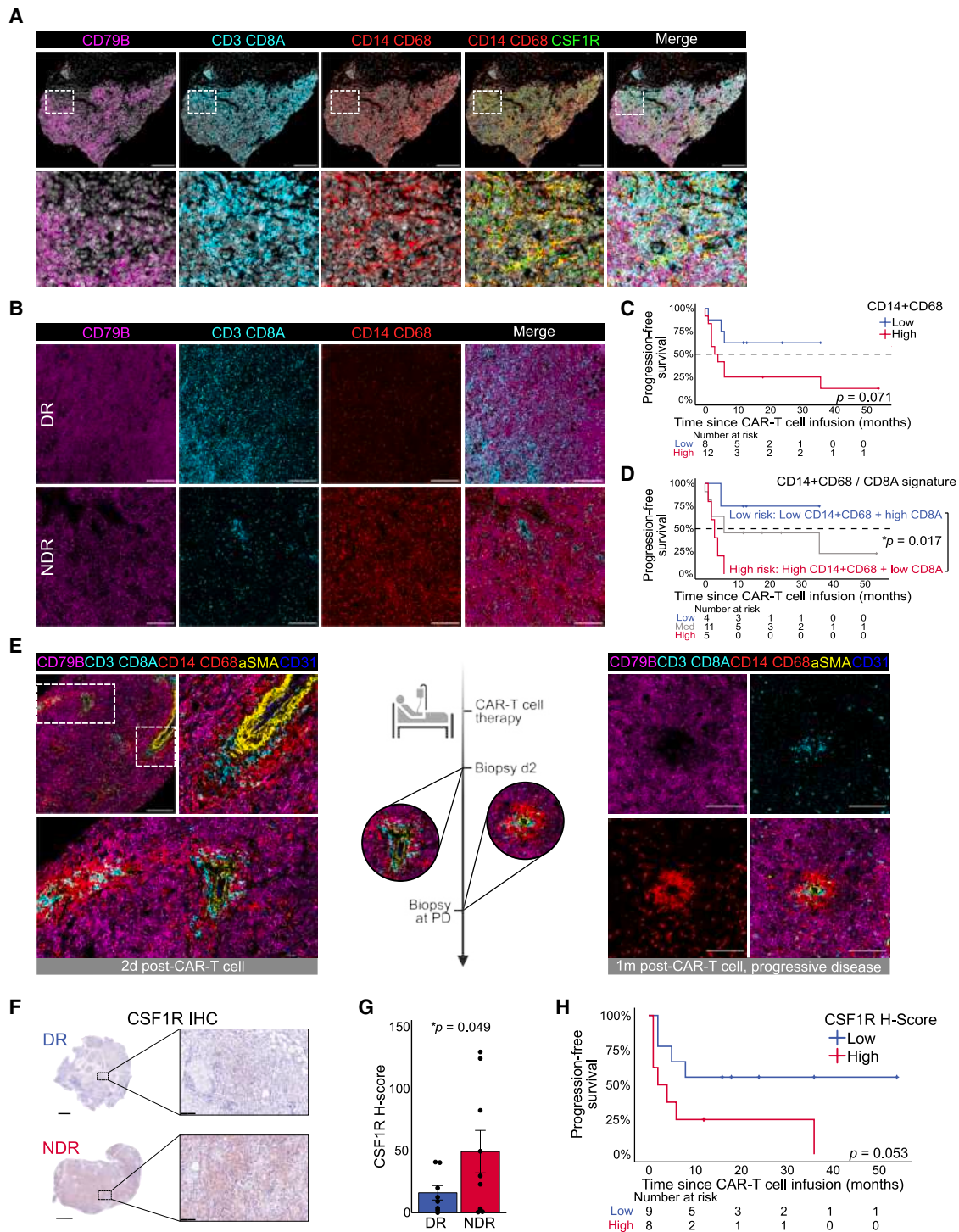


Figure 2. Proteomic profiling of aggressive B-NHL

(A) Imaging Mass Cytometry (IMC) of an aggressive B-NHL sample. Scale bar, 200 μ m.

(B–D) In-depth profiling of the TME in DR and NDR patients. (B) Representative IMC images. Scale bar, 200 μ m. (C and D) Progression-free survival (PFS) based on IMC staining for CD14+CD68 (C) and combined CD14+CD68 and CD8A (D) at baseline ($n = 20$, $p = 0.071$, $p = 0.017$, respectively, log rank test).

(E) Two highlighted regions of interest (ROIs) from a CAR-T cell-treated patient. Scale bar (left), 200 μ m. Scale bar (right), 100 μ m.

(F–H) Immunohistochemistry (IHC) validation. (F) Representative IHC images. Scale bar (overview, left), 1mm. Scale bar (zoom-in, right), 100 μ m. Summarized IHC CSF1R H-score in $n = 17$ patients based on clinical response (DR, NDR) (G) and PFS (Low CSF1R H-score <20, high CSF1R H-score >20) (H). Data are represented as means \pm SEM. Statistical significance in G was assessed using an unpaired t test (one-tailed) and in H using a log rank test. Also see [Figure S3](#), [Tables S1](#), and [S2](#).

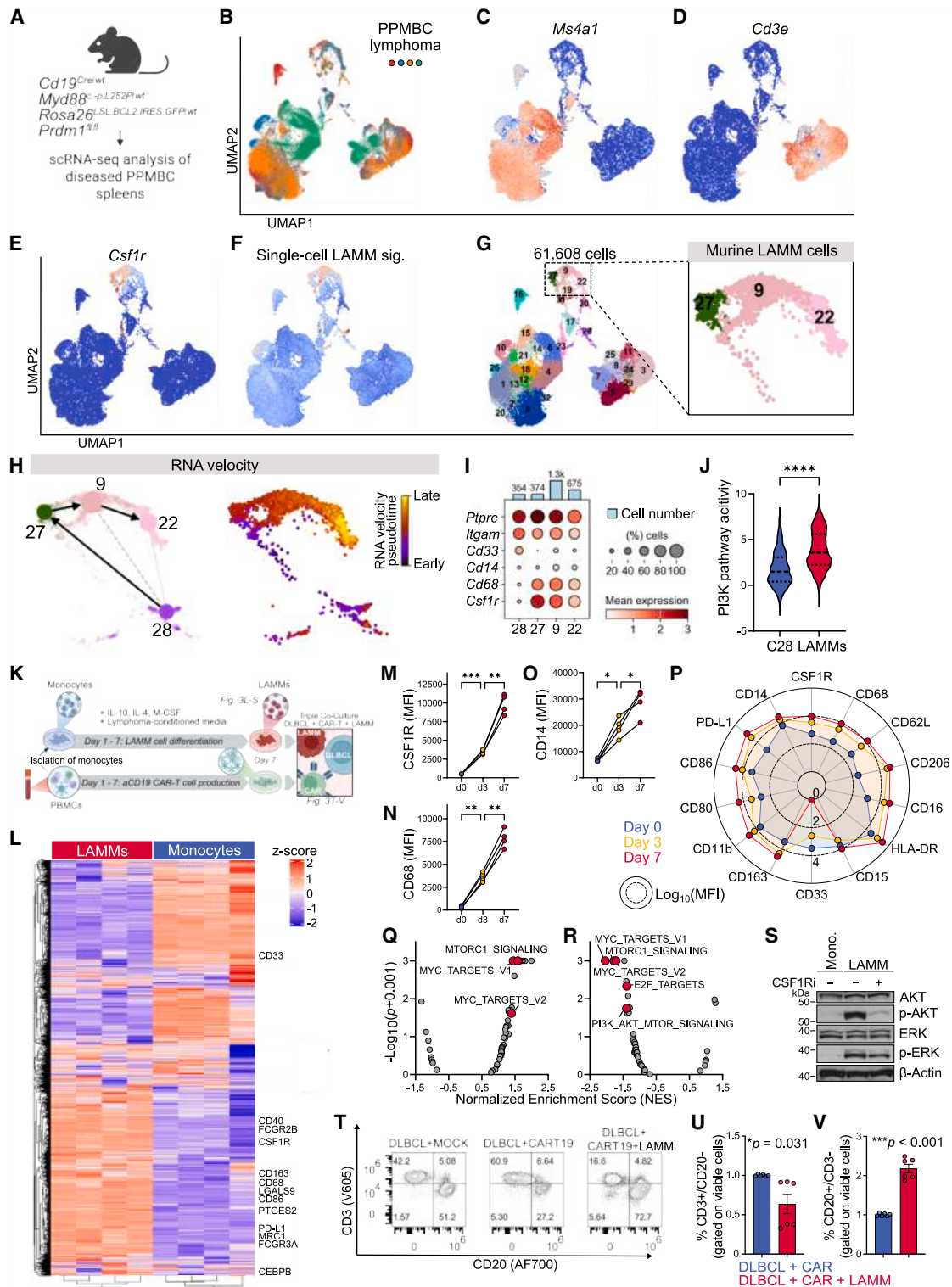


Figure 3. Development of LAMM cells relies on CSF1R-AKT signaling

(A) Genetic background of PPMBc mice.
 (B) UMAP plots for 61,608 cells from four diseased spleens of PPMBc mice.
 (C-F) UMAP plots indicating expression of *Ms4a1* (C), *Cd3e* (D), *Csf1r* (E) and LAMM gene signature (F).
 (G) Phenographic clustering of analyzed cells (left) and highlighted murine LAMM cell clusters (right).

(legend continued on next page)

To conclude, our data indicates that CSF1R⁺CD14⁺CD68⁺ LAMM cells mediate T cell exclusion potentially contributing to treatment failure of CAR-T cells in aggressive B-NHL.

CSF1R-PI3K/AKT-driven LAMM cells suppress CAR-T cell function

To independently validate our findings and characterize LAMM cells in a therapeutically relevant model, we analyzed diseased spleens from a recently established fully immunocompetent, autochthonous DLBCL mouse model harboring B cell-specific *Prdm1* aberrations on the background of oncogenic *Myd88* and *Bcl2* lesions (PPMBC: *Prdm1*^{fl/fl}, *Myd88*^{cond.p.L252P/wt}, *Rosa26*^{LSL.BCL2.IRES.GFP/wt}, *Cd19*^{Cre/wt})^{34–36} (Figure 3A). Here, we performed scRNA-seq and identified B cells (*Ms4a1*⁺), T cells (*Cd3e*⁺) and murine *Csf1r*⁺*Cd14*⁺*Cd68*⁺ LAMM cells as major populations in PPMBC-derived B-NHL (Figures 3B–3F, S4A, and S4B). Further phenographic clustering revealed three murine LAMM cell clusters (C9, C22, C27) (Figure 3G) all characterized by expression of *Csf1r*, *Cd14*, and *Cd68* (Figures S4C–S4E). To gain insight into the trajectory of LAMM cell development, we performed RNA velocity analysis and predicted a directional flow originating from a *Cd33*⁺ myeloid cell cluster (C28), which progressed toward *Csf1r*⁺*Cd14*⁺*Cd68*⁺ clusters C27, C9, and C22 (Figures 3H, 3I, and S4C–S4F). Interestingly, pathway activity analysis revealed that LAMM cell differentiation was accompanied by increased PI3K signaling (Figure 3J).

Next, we aimed to in-depth characterize the development of human LAMM cells and validate their immunosuppressive role *ex vivo*. To this end, we adapted a protocol³⁷ to generate *ex vivo* human CSF1R⁺CD14⁺CD68⁺ LAMM cells utilizing lymphoma-conditioned media (Figure 3K). Cells generated with this method were highly positive for CSF1R, CD14 and CD68, closely resembling the LAMM cell phenotype we had detected in our human and murine scRNA-seq data (Figure 3L), including a strong increase in CSF1R, CD68 and CD14 protein expression as compared to undifferentiated monocytes (Figures 3M–3O and S4G). Importantly, we did not observe differences in LAMM cell differentiation when utilizing lymphoma-conditioned media from GCB (SU-DHL-4) or non-GCB (RIVA) cell lines (Figure S4H). However, protein expression of CSF1R relied on lymphoma-conditioned media (Figure S4I). Interestingly, *ex vivo* generated human CSF1R⁺CD14⁺CD68⁺ LAMM cells presented high co-expression of CD11b, CD163 and CD206 reinforcing their immunosuppressive myeloid-monocytic phenotype³⁸ (Figure 3P), which we were able to recapitulate in murine

PPMBC mice at the scRNA-seq level (Figures S4J–S4M). At the bulk transcriptomic level and in line with our murine scRNA-seq data, development of *ex vivo* generated human CSF1R⁺CD14⁺CD68⁺ LAMM cells was accompanied by upregulation of the mTOR pathway²⁰ (Figure 3Q). In turn, treatment of differentiated *ex vivo* human CSF1R⁺CD14⁺CD68⁺ LAMM cells with CSF1R inhibition resulted in downregulation of PI3K/AKT/mTOR signaling (Figure 3R). Next, we validated our transcriptomic data via western blot analysis and found that phospho-AKT as well as phospho-ERK levels were upregulated in *ex vivo* generated human CSF1R⁺CD14⁺CD68⁺ LAMM cells. Interestingly, CSF1R inhibition mainly abrogated the phospho-AKT level, while leaving the phospho-ERK level rather unaffected (Figure 3S).

To conclude, our detailed characterization of LAMM development in PPMBC mice and *ex vivo* generated human CSF1R⁺CD14⁺CD68⁺ LAMM cells indicate that CSF1R mediates LAMM cell differentiation predominantly via PI3K/AKT signaling. Finally, to validate the CAR-T cell suppressive capacity of *ex vivo* generated human CSF1R⁺CD14⁺CD68⁺ LAMM cells, we next co-cultured *ex vivo* generated human CSF1R⁺CD14⁺CD68⁺ LAMM cells with CAR-T cells and the CD19⁺ DLBCL cell line SU-DHL-4. Strikingly, we observed a strong inhibitory effect of *ex vivo* generated human CSF1R⁺CD14⁺CD68⁺ LAMM cells on CAR-T cell expansion and cytotoxicity (Figures 3T–3V).

Cell-cell inference analysis reveals LAMM cell induced CAR-T cell suppression via EP2/4 that is abrogated in EP2/4 dual knock-out CAR-T cells

To investigate the impact of LAMM cells on CAR-T cell activity, we employed MICS to a primary human DLBCL biopsy obtained on day 8 post-CAR-T cell infusion that enabled immunofluorescent imaging of CAR⁺ T cells and in-depth analysis of the TME at subcellular resolution.³⁹ We successfully identified CAR⁺CD3⁺ T cells utilizing MICS, which separated into two clusters driven by expression of Ki67. Importantly, CAR-T cells with reduced Ki67 expression clustered with LAMM cells (Figures 4A and S5A). Supported by our IMC data, we hypothesized this phenomenon to be mainly driven by proximity. Indeed, examination of both CAR-T cell populations revealed Ki67^{low} CAR-T cells to directly interact with LAMM cells. In contrast, highly proliferating CAR-T cells with increased Ki67 expression co-localized with endogenous CAR[−]CD3⁺ T cells, while LAMM cells were excluded (Figures 4B and S5B).

(H) RNA velocity analysis of myeloid and LAMM cell clusters with indicated main vector progression (black arrow) (left) and calculated RNA velocity pseudo-time (right).

(I) Dot plot of key markers for LAMM cell differentiation.

(J) Violine plot of PI3K pathway activity analysis. Statistical significance was assessed using an unpaired *t* test (two-tailed). *****p* < 0.0001.

(K) Schematic overview.

(L) Heatmap with unsupervised clustering summarizing global protein expression (*n* = 4 donors).

(M–O) Surface expression of CSF1R (M), CD68 (N) and CD14 (O) during differentiation process (*n* = 4 donors). Statistical significance in (M–O) was assessed using an unpaired *t* test (two-tailed). **p* < 0.05, ***p* < 0.01, ****p* < 0.001.

(P) Spider plot of monocytes and LAMM cells. Shown are average expression levels from *n* = 4 donors.

(Q and R) Normalized enrichment score derived from GSEA comparing monocytes versus LAMM cells (Q) and untreated versus CSF1R inhibitor BLZ-945-treated LAMM cells (R) (*n* = 3 donors).

(S) Western blot analysis for one out of two donors.

(T) Quadrant plots indicating CD20⁺ SU-DHL-4 B-NHL cells and CD3⁺ anti-CD19 CAR-T cells. (U and V). Relative frequency of CAR-T cells (U) and lymphoma cells (V) 24 h post co-culture (*n* = 2 donors, technical triplicates). Statistical significance was assessed using a paired *t* test (two-tailed). Also see Figure S4.

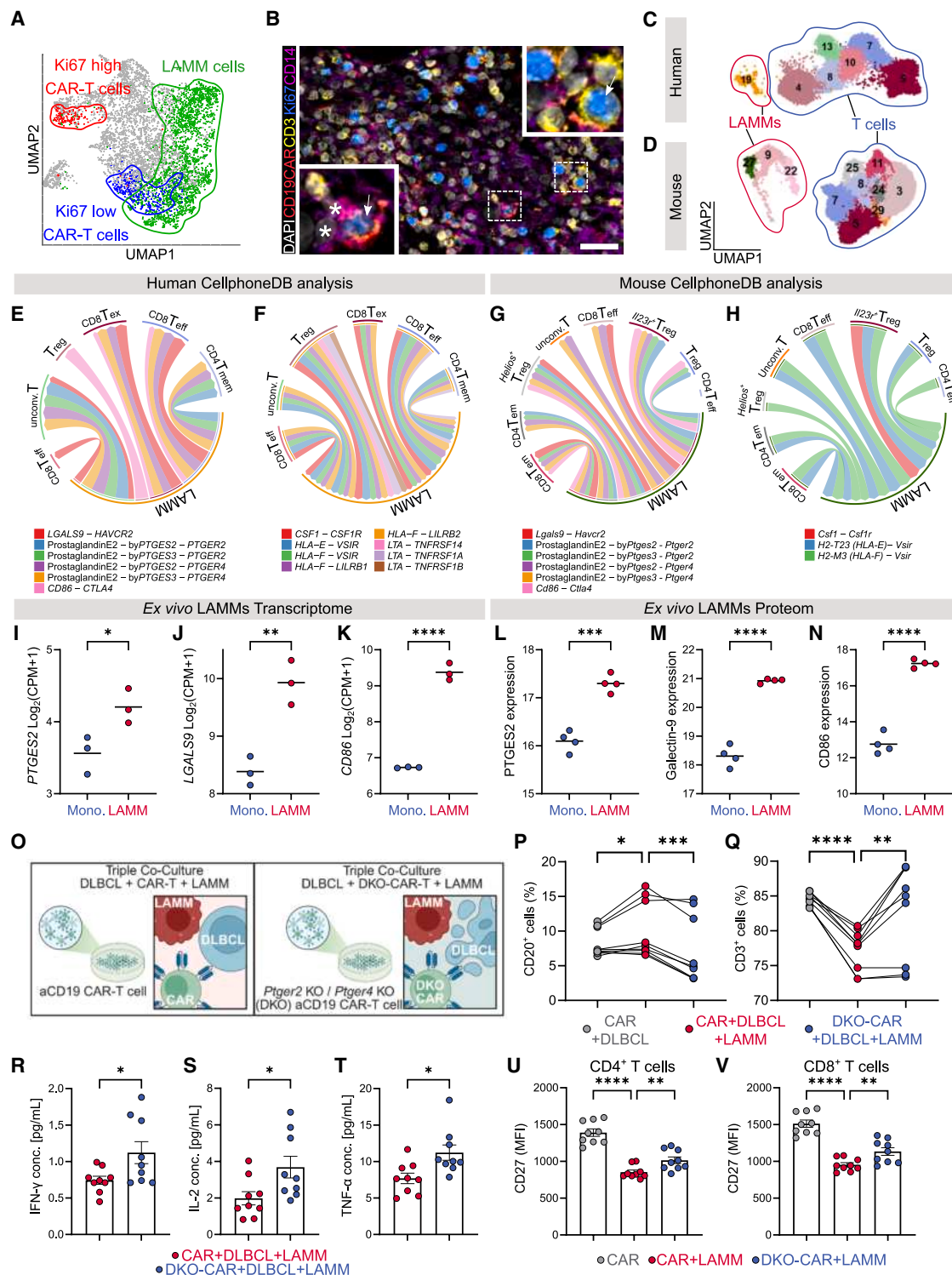


Figure 4. Characterization of LAMM-T cell interaction identifies EP2/4 dependent CAR-T cell inhibition

(A) UMAP plot from a patient sample obtained 8 days post-CAR-T cell therapy and profiled utilizing the MICS platform. Highlighted are two CAR-T cell populations in blue (non-proliferating) and red (proliferating) as well as CD14⁺CD68⁺ LAMM cells in green.

(B) Merged image of a representative area indicating the existence of proliferating CAR-T cells (white arrow, top right) without LAMM cell interaction and non-proliferating CAR-T cells (white arrow, bottom left) in close proximity to LAMM cells (white asterisks). Scale bar, 100μm.

(C and D) UMAP plots showing human (C) and murine (D) LAMM and T cell clusters. Related to [Figures 1F](#) and [3G](#) respectively.

(legend continued on next page)

To elucidate drivers of LAMM-mediated T cell suppression, we co-cultured *ex vivo* generated human CSF1R⁺CD14⁺CD68⁺ LAMM cells with CD3/CD28-activated T cells and performed a LuminexTM 48-plex cytokine screen in two independent donors. This screen identified IL-10 and CXCL9 to be among the top three differentially expressed cytokines across both donors (Figures S5C and S5D). Interestingly, *ex vivo* generated human CSF1R⁺CD14⁺CD68⁺ LAMM cells were not the primary source of IL-10 but induced IL-10 secretion in both T cells as well as CAR-T cells (Figures S5C–S5E), which is in line with our scRNA-seq data from primary human B-NHL samples. Here, IL-10 was not expressed in the LAMM cell cluster (C19) but in the T cell clusters (C4, C7, and C10) (Figures S2E and S2F).

These findings led us to further explore the interplay between both primary human and murine LAMM cells with T cells in a more unbiased manner (Figures 4C and 4D). Thus, we performed inference analysis of cell-cell communication within our scRNA-seq data utilizing the CellPhoneDB tool.⁴⁰ Our single-cell-resolved analysis revealed putative interactions of the human and murine LAMM cell clusters (human C19, murine C9, C22, and C27) with several human and murine T cell clusters including FOXP3⁺ T_{reg} cell clusters (human C4, murine C5 and C7), which are known to hinder effective anti-tumor immune responses,⁴¹ and with effector T cell clusters (human C7 and C10, murine C3) (Figures 4E–4H and S5F–S5K). Here, we found LAMM cell clusters and T_{reg} cell clusters to potentially interact via CD86-CTLA-4. CTLA-4 is known for its high relevance in maintaining the suppressive function of T_{reg} cells by diminishing the potency of antigen-presenting cells to activate other T cells.^{42,43} Furthermore, LAMM cell clusters showed potential interactions with both human and murine EOMES⁺ effector T cell clusters (human C7 and C10, murine C3) via Galectin-9 (LGALS9) putatively binding to TIM3 (HAVCR2), which has been found to define exhausted T cells in aggressive B-NHL.⁴⁴ Furthermore, we detected expression of *PTGES2* and 3 (prostaglandin E Synthase 2 and 3) in human and murine LAMM cell clusters and corresponding PGE₂ receptors EP2 (*PTGER2*) and EP4 (*PTGER4*) in human and murine T cell clusters C5, C7, C8, and C13 (human) as well as C3, C5, C7, C11, C24, C25, and C29 (murine) (Figures 4E, 4G, S5H, and S5J). Recent studies have described that PGE₂ inhibits proliferation, activity, and effector differentiation of tumor-infiltrating CD8⁺ T lymphocytes via EP2 and EP4 receptor signaling.^{45,46} These effects have been attributed to impaired IL-2 sensing and consequently mTOR pathway inactivation in human CD8⁺ tumor-infiltrating T lymphocytes.⁴⁵ Of note, gene set enrichment analysis (GSEA) of the cytotoxic T cell cluster C7 identified a downregulation of pathways involved

in protein synthesis, which are tightly regulated by mTOR signaling⁴⁷ (Figure S5L).

Vice versa, our cell-cell inference analysis indicated potential human (C4) and murine (C5 and C7) T_{reg}-mediated activation of human and murine LAMM cell clusters (human C19, murine C9, C22 and C27) respectively through HLA-E via VISTA (*VISTA*),⁴⁸ Lymphotoxin- α (*LTA*) via TNFR1/2 and HVEM (*TNFRSF1A/1B* and *14*),⁴⁹ HLA-F via VISTA (*VISTA*) and most importantly CSF1 through CSF1R expressed by all LAMM cell clusters (human C19, murine C9, C22, and C27) (Figures 4F, 4H, S5I, and S5K). In analogy, high frequency of CD4⁺CD57⁻Helios⁺ CAR-T_{reg} cells in peripheral blood of aggressive B-NHL patients on day 7 post infusion have been associated with worse treatment outcomes.⁹ We hypothesized that these prognostically relevant CD4⁺CD57⁻Helios⁺ CAR-T_{reg} cells – similar to endogenous T_{reg} cells – are capable of LAMM cell activation. Intriguingly, we found both the frequency and the expression level of CSF1 to be elevated in CD4⁺CD57⁻Helios⁺ CAR-T_{reg} cells as compared to other CAR-T cells in refractory CAR-T cell treated patients (Figure S5M).

Finally, we aimed to functionally validate insights gained from cell-cell inference analysis in *ex vivo* generated human CSF1R⁺CD14⁺CD68⁺ LAMM cells. To this end, we first validated RNA expression of *PTGES2*, *LGALS9*, and *CD86* (Figures 4I–4K) as well as protein expression of Prostaglandin E Synthase-2, Galectin-9 and CD86 (Figures 4L–4N) in monocytes and differentiated *ex vivo* human CSF1R⁺CD14⁺CD68⁺ LAMM cells. Here, we identified that all were increased in differentiated *ex vivo* human CSF1R⁺CD14⁺CD68⁺ LAMM cells as compared to monocytes (Figures 4I–4N). Next, we performed dual knock-out of the PGE₂ receptors EP2/EP4 via CRISPR/Cas9 editing in anti-CD19 CAR-T cells to abolish suppression via PGE₂ in our co-culture system (Figure 4O). Strikingly, when co-culturing dual knock-out (DKO) CAR-T cells with *ex vivo* generated human CSF1R⁺CD14⁺CD68⁺ LAMM cells and SU-DHL-4 cells, we observed improved tumor cell killing and higher T cell expansion with DKO anti-CD19 CAR-T cells versus unedited anti-CD19 CAR-T cells (Figures 4P and 4Q). Moreover, in our co-culture system DKO anti-CD19 CAR-T cells secreted more IFN- γ , IL-2 and TNF- α as compared to unedited anti-CD19 CAR-T cells (Figures 4R–4T) and showed higher levels of the activation marker CD27 (Figures 4U and 4V).

Thus, CSF1R⁺CD14⁺CD68⁺ LAMM cells seemed to directly inhibit endogenous T cell and CAR-T cell proliferation as well as cytotoxicity, by expressing T cell-suppressive ligands and secretion of inhibitory cytokines.

(E–H) CellPhoneDB analysis highlighting interactions of the human LAMM cell cluster with T cells clusters (E: LAMM-Ligand:T cell-Receptor, F: LAMM-Receptor:T Cell-Ligand) and combined murine LAMM cell clusters with T cell clusters (G: LAMM-Ligand:T cell-Receptor, H: LAMM-Receptor:T Cell-Ligand).

(I–K) RNA expression levels of *PTGES2* (I), *LGALS9* (J) and *CD86* (K) in monocytes and differentiated LAMM cells identified via bulk RNA-seq.

(L–N) Protein expression levels of *PTGES2* (L), Galectin-9 (M) and CD86 (N) in monocytes and differentiated LAMM cells. Statistical significance in (I–N) was assessed using an unpaired *t* test (two-tailed). **p* < 0.05, ***p* < 0.01, ****p* < 0.001, *****p* < 0.0001.

(O) Schematic overview of co-culture experiments.

(P and Q) Flow cytometry-based assessment of CD20⁺ SU-DHL-4 cells (P) and CD3⁺ T cells (Q). Statistical significance was assessed using a paired *t* test (two-sided). **p* < 0.05, ***p* < 0.01, ****p* < 0.001, *****p* < 0.0001.

(R–T) Cytokine secretion of IFN- γ (R), IL-2 (S) and TNF- α (T). Data are represented as means \pm SEM. Statistical significance was assessed using an unpaired *t* test (two-tailed). **p* < 0.05.

(U and V) Surface CD27 expression. Data are represented as means \pm SEM. Statistical significance was assessed using an unpaired *t* test (two-tailed). ***p* < 0.01, *****p* < 0.0001. Also see Figure S5.

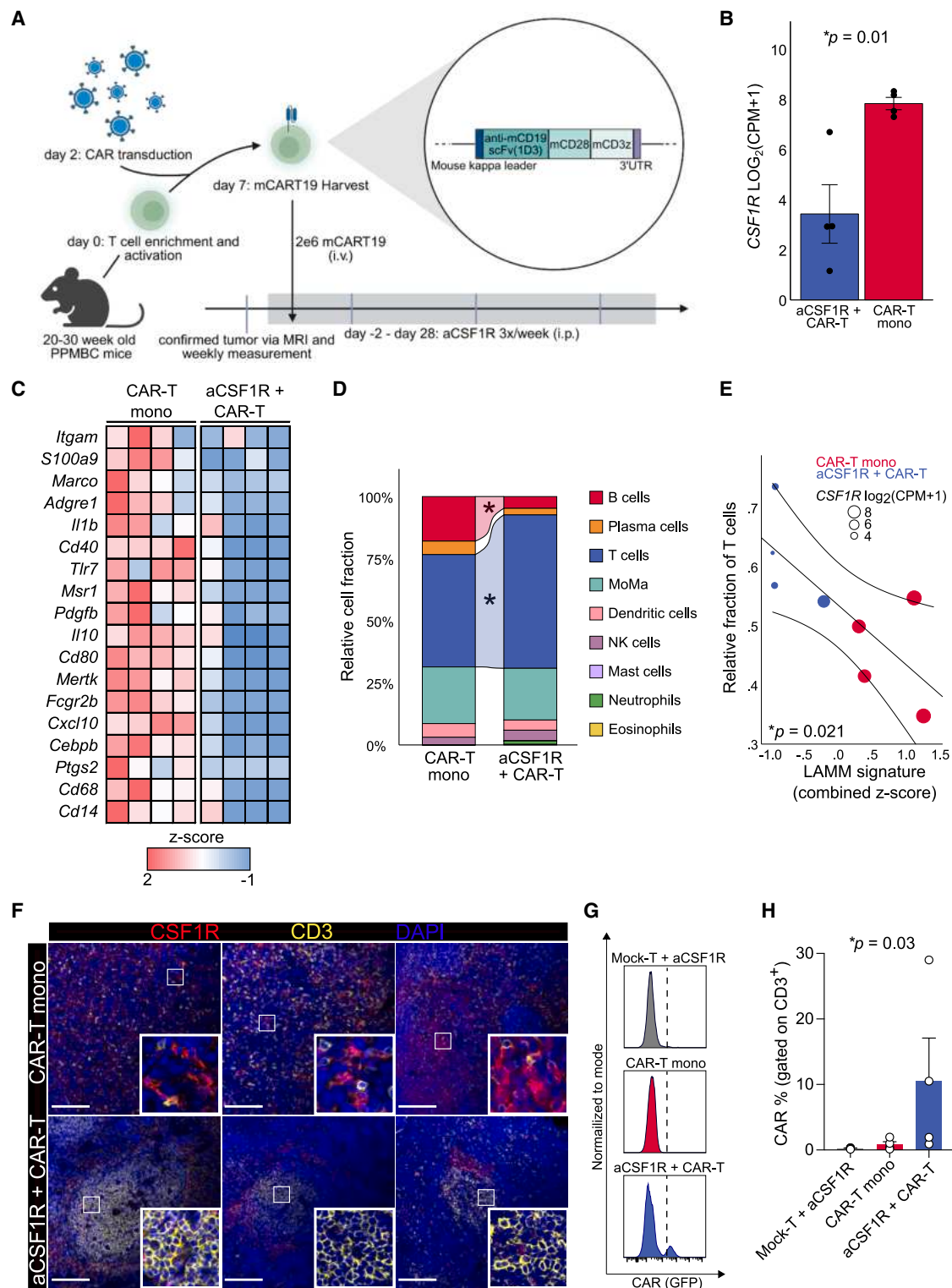


Figure 5. CSF1R⁺ LAMM cell depletion enhances CAR-T cell expansion

(A) Schematic study overview.

(B) *Csf1r* expression in treated mice. Data are represented as means \pm SEM. Statistical significance was assessed using an unpaired *t* test (two-tailed).

(C) Heatmap of gene expression measured by bulk RNA-seq from spleens of CAR-T cell-treated and successfully aCSF1R + CAR-T cell-treated PPMBc mice ($n = 8$).

(D) Inference of immune cell fractions via CIBERSORTx^{33,50} analysis. Statistical significance was assessed using an unpaired *t* test (two-tailed). * $p < 0.05$.

(legend continued on next page)

CSF1R inhibition converts the immunosuppressive TME into an immunosupportive one and enhances CAR-T cell expansion *in vivo*

Triggered by our finding that suppressive CSF1R⁺CD14⁺CD68⁺ LAMM cells relied on CSF1R signaling for differentiation and impaired CAR-T cell function, we sought to investigate the effect of CSF1R inhibition on the composition of the TME and CAR-T cell response in our fully immunocompetent, autochthonous DLBCL mouse model. Of note, high tumor volume (HTV) PPMBC tumors faithfully recapitulate the aggressive phenotype of NDR patients in our clinical cohort with high expression of LAMM signature genes (Figures S6A and S6B), an enrichment of hypoxia, glycolysis, and reactive oxygen species pathways (Figures S6C–S6E), as well as worse outcome to CD19 CAR-T cell therapy in comparison to low tumor volume (LTV) PPMBC mice (Figures S6F and S6G).

Given the transcriptomic and clinical resemblance of HTV PPMBC mice with NDR CAR-T cell-treated aggressive B-NHL patients, we initiated treatment of HTV animals with an anti-CSF1R antibody on day –2, followed by a single infusion of 2×10^6 murine anti-CD19 CAR-T cells on day 0. All mice were monitored weekly via repetitive MRI scans and mice were sacrificed to analyze lymphoma-bearing spleens at the end of treatment (Figure 5A). Transcriptomic analysis of spleen samples from CAR-T cell versus aCSF1R + CAR-T cell-treated mice revealed a downregulation of the LAMM gene signature as well as CSF1R, but did not affect expression of M2 macrophage-related genes (Figures 5B, 5C, and S6H). Of note, expression of *Csf1r* and LAMM signature genes showed a strong correlation indicating target-dependent LAMM cell depletion (Figure S6I). Next, we employed CIBERSORTx^{33,50} analysis to infer compositional changes in the TME. Here, we observed a strong increase of T cells within the TME of aCSF1R + CAR-T cell as compared to CAR-T cell-treated PPMBC mice (Figure 5D). Strikingly, the T cell fraction interrogated via CIBERSORTx^{33,50} showed a strong negative correlation with both the LAMM gene signature and *Csf1r* expression (Figures 5E and S6J). To validate our transcriptomic analysis, we performed immunofluorescence (IF) analysis and confirmed successful staining of CSF1R in LAMM cells along with strong T cell infiltration (Figures 5F and S6K). Finally, we aimed to evaluate the impact of concomitant CSF1R blockade on intratumoral CAR-T cell expansion. To this end, we analyzed spleen samples via flow cytometry and detected enhanced CAR-T cell expansion in aCSF1R + CAR-T versus CAR-T cell mono-treated mice (Figures 5G, 5H and S6L). Together, our data indicates conversion of the TME accompanied by enhanced expansion of both endogenous and CAR-T cells in HTV PPMBC mice, when treated with a combination of aCSF1R + CAR-T cells.

CSF1R blockade combined with CAR-T cells induces a T cell-rich follicular architecture and vessel normalization

Encouraged by our IF-based pilot study, we next applied IMC to obtain more detailed insights into the TME under treatment with aCSF1R + CAR-T cells (Figure 6A; Table S2). Combination therapy with aCSF1R + CAR-T cells resulted in a restored follicular architecture of spleens from HTV PPMBC mice along with reduced B cell load, but enhanced CD4⁺ and CD8⁺ T cell infiltration (Figures 6A–6C). We further characterized these follicles and identified strong expression of CD3, CD4, and CD8. While central areas of T cell-rich follicles were frequently positive for both CD4 and CD8, peripheral regions were mainly CD4 positive. Most importantly, LAMM cells were excluded from T cell-rich clusters (Figures 6D and 6E) as indicated by long cell-to-cell distance between LAMM and T cells (Figures 6F and S7A–S7C).

Our patient-derived transcriptomic data showed strong enhancement of angiogenic factors related to hypoxia along with insufficient tumor vessel priming in patients with NDR (Figures S1–S1K), and HTV PPMBC mice recapitulated these findings (Figures S6C–S6E). Furthermore, myeloid-monocytic immunosuppressive cells have been largely described to secrete angiogenic factors inducing a highly insufficient, disorganized tumor vessel architecture known to impair priming, infiltration, and expansion of cytotoxic T cells.⁵¹ Thus, we asked whether treatment with aCSF1R + CAR-T cells can successfully reverse hallmarks of tumor angiogenesis. To this end, we analyzed bulk transcriptomic data and found genes associated with tumor vessel normalization (*Cd34*, *Cldn5*, *Pecam1*, and *Vwf*) to be enriched (Figure S7D) upon aCSF1R + CAR-T cell treatment. In line with these findings, we observed downregulation of hypoxia-related pathways in aCSF1R + CAR-T cell-treated mice as compared to CAR-T cell-treated mice (Figures 6G, S7E, and S7F). Ultimately, we independently confirmed tumor vessel normalization utilizing IMC. In CAR-T cell-treated HTV PPMBC mice insufficient priming of tumor vessels was characterized by low pericyte coverage and a diffuse distribution of CD31⁺ endothelial cells. In contrast, we observed completely normalized tumor vessel structure in mice treated with aCSF1R + CAR-T cells as indicated by a normalized tumor vasculature accompanied by larger diameter and a highly increased pericyte coverage (Figure 6H).

Thus, our *in vivo* data indicates vast remodeling of the TME, when CSF1R inhibition is combined with CAR-T cells. In addition, we have highlighted a dysfunctional tumor microvessel-promoting function of CSF1R⁺ LAMM cells, which can be overcome by CSF1R inhibition. In turn, tumor vessel normalization with high coverage of well-organized pericytes has been shown to improve blood flow, endothelial function, as well as infiltration and expansion of cytotoxic T cells.⁵²

(E) Correlation of relative T cell infiltration defined using CIBERSORTx^{33,50} and LAMM signature from bulk transcriptomic analysis (Spearman's $r = -0.786$, $^*p = 0.021$).

(F) Immunofluorescence staining of spleen samples from CAR-T cell-treated (upper row) and successfully aCSF1R + CAR-T cell-treated (lower row) PPMBC ($n = 3$ independent mice per group, DAPI: blue, CSF1R: red, CD3: yellow). Scale bar, 100 μ m.

(G and H) Representative histograms (G) and summarized CAR frequency (H) of CAR-T cells in spleens from treated mice ($n = 4$ per treatment group). Data are represented as means \pm SEM. Statistical significance was assessed using a Kruskal-Wallis test. Also see Figure S6.

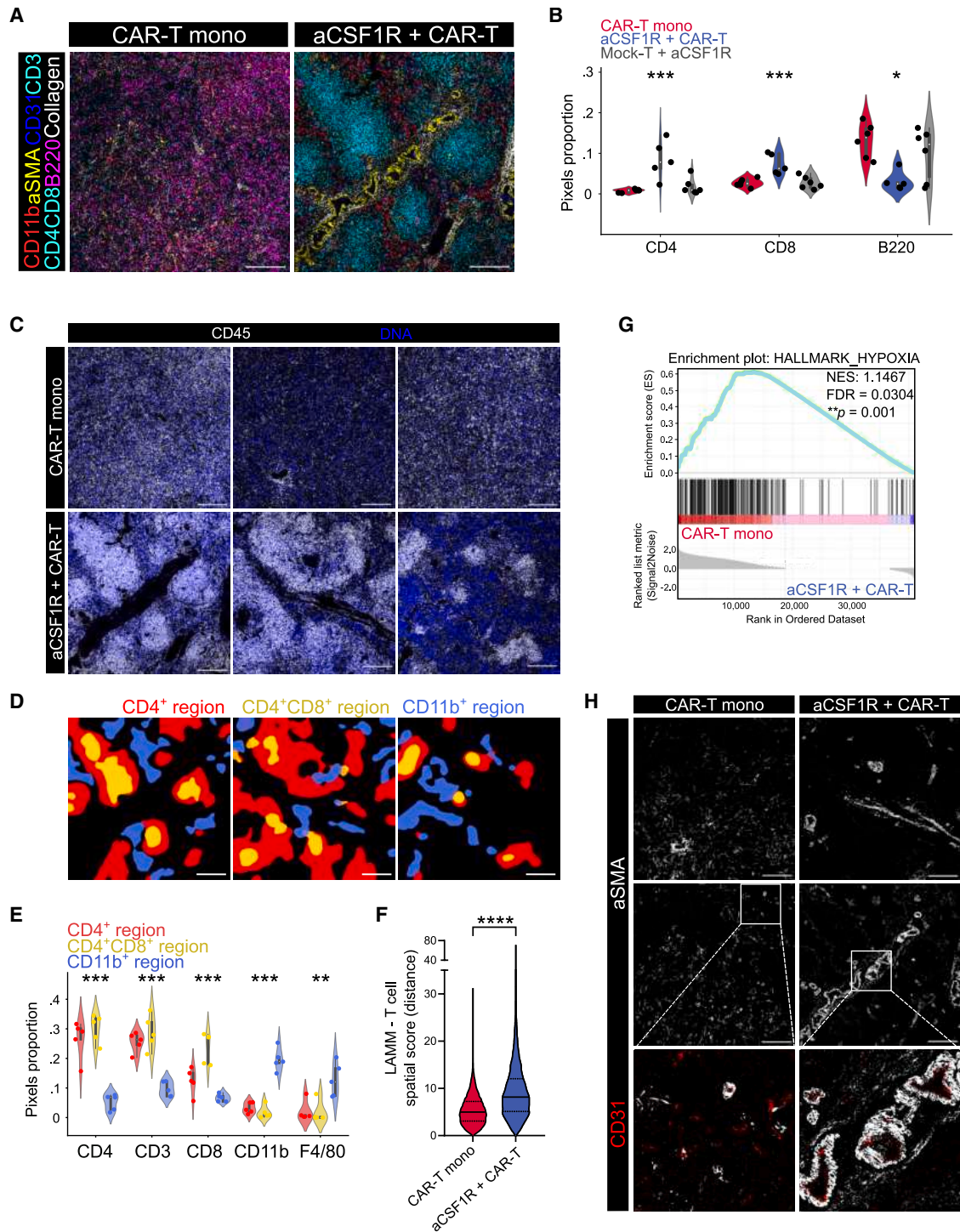


Figure 6. TME reprogramming after aCSF1R + CAR-T cell treatment

(A) Representative Imaging Mass Cytometry (IMC) images from treated PPMBc mice. Scale bar, 200 μ m.

(B) Distribution of pixel proportion for $n = 3$ CAR-T cell-treated and Mock-T cells + aCSF1R-treated mice respectively (2 ROIs per diseased spleen) as well as $n = 5$ aCSF1R + CAR-T cell-treated mice (1 ROI per diseased spleen). Statistical significance was assessed using One-way ANOVA. * $p < 0.05$, *** $p < 0.001$.

(C) CD45 and cell nucleus staining (images from $n = 3$ independent mice per group). Scale bar, 200 μ m.

(D) Enriched regions of CD11b, CD4 and CD8 and their intersection on the same ROIs as aCSF1R + CAR-T cell-treated ROIs from panel C. Cell neighborhood and area analysis from responding aCSF1R + CAR-T cell-treated mice ($n = 3$ independent mice). Scale bar, 200 μ m.

(E) Distribution of pixel proportion within indicated immune cell areas from D across $n = 5$ independent aCSF1R + CAR-T cell-treated mice. Statistical significance was assessed using One-way ANOVA. ** $p < 0.01$, *** $p < 0.001$.

(legend continued on next page)

CSF1R inhibition displays synergistic treatment effects in combination with CAR-T cells

Finally, we aimed to evaluate the impact of aCSF1R in combination with CAR-T cells on disease response and survival of PPMBC mice. We monitored tumor volumes by longitudinal MRI scans and found that CAR-T cells alone and aCSF1R + Mock-T cell treatment resulted in uncontrolled tumor growth as evidenced by an increase in spleen size due to massive lymphomatous infiltration. In comparison, aCSF1R + CAR-T cell treatment yielded powerful responses, in some instances with normalized spleen size post treatment (Figures 7A and 7B). Most strikingly, we observed a significant improvement of PFS in HTV PPMBC mice treated with aCSF1R + CAR-T cells compared to treatment with CAR-T cells alone (Figure 7C). Of note, the addition of the CSF1R inhibitor improved the number of DR with long-lasting, complete remissions, which resulted in a significantly prolonged OS as compared to mice treated with CAR-T cells alone (Figure 7D). As our clinical data indicate an impact of initial tumor burden on CAR-T cell response (Figures S1B and S1C), we analyzed PFS and OS in aCSF1R + CAR-T cell-treated mice based on tumor size before treatment and here identified no survival differences (Figures S7G and S7H). Given the long-lasting complete remissions in some aCSF1R + CAR-T cell-treated mice, we investigated potential side effects by combining CSF1R inhibition with CAR-T cells and, thus, analyzed the expression of key cytokines that have been related to cytokine release syndrome (CRS) and immune effector cell-associated neurotoxicity syndrome (ICANS). Interestingly, expression levels of these cytokines were downregulated in samples from mice treated with aCSF1R + CAR-T cells as compared to CAR-T cells alone (Figure S7I).^{53,54} In summary, we report a synergistic treatment effect by combining CAR-T cell therapy and CSF1R inhibition, which was well-tolerated and led to prolonged survival in an autochthonous DLBCL mouse model.

DISCUSSION

Applying high-dimensional profiling we uncover a distinct CSF1R⁺CD14⁺CD68⁺ LAMM cell population that inhibits CAR-T cell proliferation and cytotoxicity. Furthermore, LAMM cell infiltration in pretreatment specimens of B-NHL patients is associated with NDR to CAR-T cell therapy and poor clinical outcome. Finally, we demonstrate *in vivo* that CSF1R blockade bears the potential to convert the immunosuppressive into an immunosupportive TME, to restore anti-lymphoma immunity, and thereby enhance CAR-T cell response. Previous work has successfully demonstrated how malignant B cells evade the CAR-T cell attack, for instance, by antigen downregulation or downregulation of pro-apoptotic genes,^{5,55} and established a molecular framework to design novel T cell therapies equipped with synthetic immunoreceptors.^{5,56,57} In addition, recent work has demonstrated the clinical relevance of hypoxia-dependent, immunosuppressive signaling by myeloid cells in the context of a diminished activity

of CAR-T cells in lymphoma.^{10,12,13} Importantly, additional work is needed to understand whether these recently identified resistance mechanisms and/or LAMM cell-dependent factors limit response of our combined treatment approach and how they can be overcome.

Our work expands on the current concepts of myeloid cells inhibiting CAR-T cell function within the TME in aggressive B-NHL. After confirming that a myeloid-monocytic gene signature predicts response to CAR-T cell treatment, our scRNA-seq analyses of human B-NHL revealed the presence of an LAMM cell population expressing CD14, CD68 as well as CSF1R prior to CAR-T cell therapy, which is linked to CAR-T cell failure. At the proteomic level, we validated this finding via IMC. Strikingly, we show that targeted reprogramming of the TME via CSF1R blockade creates a supportive niche for CAR-T cells in aggressive B-NHL. CSF1/CSF1R signaling has been identified as the main regulator of myeloid-monocytic cell differentiation and to mediate immunosuppressive functions within the TME.^{32,58–60} Previous work described that CSF1R induces polarization toward an immunosuppressive M2-like macrophage phenotype in an indolent lymphoma model.⁶¹ Furthermore, studies indicated a potential impact of CSF1R⁺ macrophages on T cell exclusion in solid tumor models.⁶² To elaborate on LAMM-T cell interaction at a molecular level, we performed inference analysis of cell-cell communication which revealed that LAMM cells exert their immunosuppressive function by direct interaction with cytotoxic T cells via *PTGES2* and *3* in LAMM cells and the corresponding PGE₂ receptors EP2 and EP4 in both human and murine effector T cell clusters.^{45,46} Importantly, we could show that CRISPR/Cas9-based editing of both EP2 and EP4 in anti-CD19 CAR-T cells enhanced their activation, cytokine secretion and tumor cell killing in the presence of *ex vivo* generated human CSF1R⁺CD14⁺CD68⁺ LAMM cells. These results underscore recently published data highlighting the PGE₂-EP2/EP4 signaling axis as a key mechanism of IL-2 unresponsiveness and consequently T cell impairment.^{45,46} Together, our data expand on these findings in the context of aggressive B-NHL, outlining potential LAMM cell-dependent, PGE₂-mediated (CAR-) T cell dysfunction. Moreover, our cell-cell inference analysis revealed T_{reg}-mediated activation of LAMM cells via CSF1-induced activation of CSF1R on LAMM cells. While our data show that LAMM cells induce T cell exclusion, this functional interaction between T_{reg} cells and LAMM cells might reflect the early dependence of LAMM cells on T_{reg} cells when shaping an immunosuppressive TME prior to the exclusion of T cells. We could further confirm in an independent patient cohort a high frequency of CD4⁺Helios⁺CSF1⁺ CAR-T_{reg} cells in peripheral blood of CAR-T refractory aggressive B-NHL patients adding further evidence to CD4⁺Helios⁺CSF1⁺ CAR-T_{reg} cells mediating LAMM cell activation.⁹

While our work has focused on the TME, hypoxia-induced suppressive myeloid cells in the TME have a long-established role in tumor immunology.^{63–65} In healthy tissue, classical monocytes (cMo) express S100A9 similar to LAMM cells,

(F) Violin plot indicating spatial score as a metric of LAMM-T cell distance in spleens from CAR-T cell ($n = 3$ samples, 2 ROIs per samples) versus aCSF1R + CAR-T cell treated mice ($n = 5$ samples, 1 ROI per sample). Statistical significance was assessed using an unpaired *t* test (two-tailed). **** $p < 0.0001$.

(G) GSEA in CAR-T cell versus aCSF1R + CAR-T cell-treated mice.

(H) Representative aSMA and CD31 staining. Images from two independent mice. Scale bar, 200 μ m. Also see Figure S7 and Table S2.

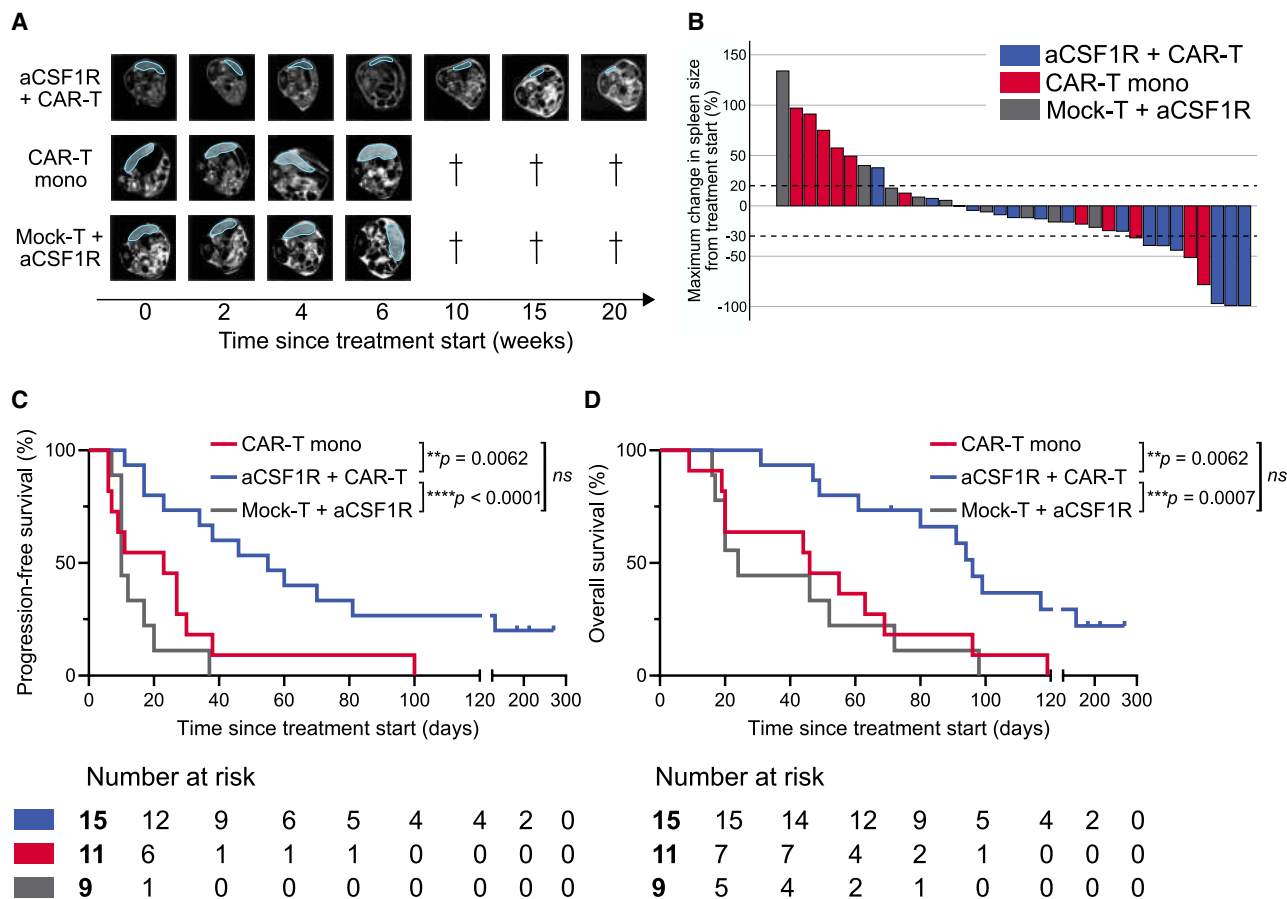


Figure 7. CSF1R inhibition displays synergistic efficacy in combination with anti-CD19 CAR-T cell therapy

(A) Representative MRI images of PPMBC mice treated as indicated.

(B) Waterfall plot of tumor shrinkage.

(C and D) Progression-free (PFS) (C) and overall survival (OS) (D) in PPMBC mice treated as indicated. Statistical significance was assessed using log rank test. $^{**}p < 0.01$, $^{***}p < 0.001$, $^{****}p < 0.0001$. Also see [Figure S7](#).

potentially indicating that LAMM cells arise from cMo.⁶⁶ However, it has yet to be determined if myeloid cells in other tumors share co-expression of CSF1R, CD14 as well as CD68 and are driven by CSF1R-mediated PI3K/AKT signaling. Recently, targeting of CSF1R has been shown to improve the efficacy of several immunotherapeutic approaches^{67–69} or even demonstrated single agent activity in glioblastoma tumor models,⁷⁰ although with limited therapeutic efficacy due to post-treatment fibrosis.⁷¹ With the advent of single-cell technologies, pan-cancer and cross-tissue studies have provided insights into the heterogeneity and plasticity of myeloid cells found in the TME,^{66,72} thus highlighting the need for future investigations to carefully dissect identity, fate, and therapeutic relevance of myeloid-monocytic cells in other tumors especially in the context of emerging CAR-T cell therapies for solid tumors.

CRS and ICANS are major complications after anti-CD19 CAR-T cell therapy for aggressive B-NHL and are associated with high morbidity.^{1–4,73,74} Our data show that CSF1R inhibition suppresses the secretion of cytokines related to CRS and ICANS confirming recent preclinical work demonstrating that CSF1R inhibition improves ICANS severity.⁷⁵

In summary, we uncover a CSF1R⁺ myeloid-monocytic cell population that mediates an immunosuppressive TME and drives CAR-T cell resistance in aggressive B-NHL. Therapeutic inhibition of CSF1R in combination with anti-CD19 CAR-T cell therapy converts an immunosuppressive TME into a T cell-enriched TME and displays synergistic treatment efficacy. As CSF1R inhibitors have already been clinically evaluated and FDA-approved,^{76–79} this therapeutic combination has the potential for rapid translation into patient care. Thus, we propose to test the combination of anti-CD19 CAR-T cells with CSF1R inhibition in clinical studies for patients suffering from *r/r* aggressive B-NHL.

RESOURCE AVAILABILITY

Lead contact

Reasonable requests for information and resources may be directed to Roland T. Ullrich (roland.ullrich@uk-koeln.de).

Materials availability

This study did not generate new reagents.

Data and code availability

The bulk RNA-seq and single-cell RNA-seq data as well as the proteomic data of the *ex vivo* generated LAMM cells have been deposited on Zenodo with an identifier of <https://doi.org/10.5281/zenodo.15280550>.

ACKNOWLEDGMENTS

We thank all study participants who provided primary material and Marek Franitz, Marion Müller, Alexandra Florin, Wiebke Jeske, Uschi Zenz, Petra Hoffmann, and Mehrnaz Babaki for technical support.

This study was supported by: the Deutsche Forschungsgemeinschaft (German Research Foundation) grant 455784452 as part of CRC1530 (with project funding for H.C.R. (A01), M.H. (B01, Z01), C.P. (B02), R.T.U./M.C. (B05), R.D.J. (C02), R.B. (Z02), and N.A. (Z03)), grant 555464052 to H.B.-W., grant 413326622 as part of CRC1399 to J.B. and H.C.R., grant 325931972 as part of CRC1310 to J.B., grant 424228829 as part of CRC1430 to H.C.R., grant RE2246/16-1 to H.C.R., grant KO5055/2-1 and KO5055/3-1 to S.K., grant UL379/1 to R.T.U., funding as part of CRC1403 to J.R., funding as part of CRC-TRR338/1 2021–452881907 to S.K., grant INST216/512/1FUGG to the Regional Computing Center of the University of Cologne, grant INST216/1174-1FUGG to the CMMC Microscopy Service and funding as part of projects 407493903 and 423957469 to the West German Genome Center; the Deutsche Krebshilfe (German Cancer Aid) grant 70113307 (Mildred Scheel Nachwuchs Zentrum) to D.S., D.B., R.F., J.-M.H., P.J.B., and J.B., grant 1117240 and 70113041 to H.C.R., grant 70113009 to R.T.U. and AvantCAR.de to S.K.; the Else Kröner-Fresenius Foundation (EKFS) grant 2020_EKFK.19 (Else Kröner Forschungskolleg Clonal Evolution in Cancer, Cologne, Germany) to D.S. and J.-M.H., an EKFS Excellence Stipend to P.J.B. and EKFS/IOLIN to S.K.; the Ministry of Culture and Science of the State of Northrhine Westphalia (Germany) grant 005-1901-0038 as part of the Cancer Center Cologne Essen to M.H. and H.B.-W. and the CANTAR network (NW21-062B) funded through the program “Netzwerke 2021” to J.B. and H.C.R.; Köln Fortune grant 494/2020 and the Faculty of Medicine Cologne (Gerok Projekt 12/2019) to P.G.; the ERA-PerMed program (HighRisk-HighGain consortium) to H.C.R.; the Bavarian Cancer Research Center (BZKF, TANGO), Marie Skłodowska-Curie Training Network for Optimizing Adoptive T Cell Therapy of Cancer (funded by the Horizon 2020 programme of the European Union; grant 955575), the Wilhelm Sander-Stiftung, the Go-Bio-Initiative, the m4-Award of the Bavarian Ministry for Economical Affairs, Bundesministerium für Bildung und Forschung (CONTRACT and Binostics), European Research Council (Starting Grant 756017, PoC Grant 101100460 and CoG 101124203), Dr.-Rurainki Foundation, Fritz Bender Foundation, Deutsche José Carreras Leukämie-Stiftung, Hector Foundation, Bavarian Research Foundation (BAYCELLATOR), the Bruno and Helene Jöster Foundation (360° CAR) and the Monika Kutzner Foundation for Cancer Research to S.K.; the German Center for Infection Research (DZIF, TTU-TB grants 02.806, 02.814 and 02.913), the German Federal Ministry of Education and Research (BMBF, grant IdEpiCo), and the European Union Innovative Medicines Initiative 2 Joint Undertaking program grant no. 853989 (ERA4TB) to J.R.; the CMMC (B10) to S.J.T. and J.R.; and the Imhoff Stiftung, the Köln Fortune Program and the Jubiläumstiftung 1988 (University of Cologne) to S.J.T.

AUTHOR CONTRIBUTIONS

D.S., P.G., and H.B.-W. designed the study, performed experiments, analyzed data and wrote the manuscript. R.G., F.R., K.B., and N.A. performed computational analyses. P.S., L.T., M.K., J.D., L.G., D.B., A.G.S., Z.G., J.J., B.H., M.N., R.F., T.R., D.L., S.J.B., H.B., C.-A.V., N.P., L.S., M.F., S.W.-R., A.-I.I., J.-M.H., H.L., J.K.S., and J.P. performed experiments and analyzed data. P.J.B., R.D.J., G.K., S.B., S.M.-B., C.P., M.P., J.R., A.Q., M.N., J.B., W.M., T.P., K.B., S.J.T., R.B., T.O., M.H., S.K., M.C., H.C.R., C.M., N.A., and P.B. analyzed data and provided resources. R.T.U. designed and supervised the study and wrote the manuscript. All authors read, revised and approved the manuscript.

DECLARATION OF INTERESTS

H.B.-W. received research funding from Wilson Wolf Manufacturing, LLC (G-Rex Grant Program). H.C.R. received consulting and lecture fees from Abbvie,

AstraZeneca, Vertex, and Merck, received research funding from AstraZeneca and Gilead Pharmaceuticals and is a co-founder of CDL Therapeutics GmbH. J.-M.H. received research funding from Incyte, MorphoSys, and Novartis, received honoraria and/or is an advisor or consultant for Incyte, SERB Pharmaceuticals, SOBI, Novartis, Genmab, and Miltenyi Biotec, and received travel support from Novartis, SERB pharmaceuticals, and SOBI. J.B. received research funding from Bayer and for travel from Merck outside of the submitted work. A.-I.I. is part of the speakers' bureau at Philips Healthcare. S.K. received honoraria from Cymab, Plectonic, TCR2 Inc., Novartis, BMS, Miltenyi, and GSK, is inventor of several patents in the field of immuno-oncology, received license fees from TCR2 Inc. and Carina Biotech, and received research support from TCR2 Inc., Plectonic GmbH, Catalym GmbH, Arcus Bioscience, and Tabby Therapeutics for work unrelated to the manuscript. The remaining authors declare no competing interest.

STAR★METHODS

Detailed methods are provided in the online version of this paper and include the following:

- **KEY RESOURCES TABLE**
- **EXPERIMENTAL MODEL AND STUDY PARTICIPANT DETAILS**
 - Patient cohorts and samples
 - Cell lines
 - Experimental mice
- **METHOD DETAILS**
 - Quantitative PET analysis
 - Cell culture
 - Human and murine anti-CD19 CAR-T cells
 - Bulk RNA-seq of human and murine samples
 - Bulk RNA analysis of human and murine samples
 - Global protein profiling
 - Global protein analysis
 - Western blot
 - Droplet-based scRNA-seq of human and murine samples
 - Single-cell data pre-processing
 - Single-cell unsupervised clustering
 - Differential gene analysis
 - Cell-cell interactions
 - RNA velocity analysis
 - Gene set enrichment analysis
 - Pathway activity analysis
 - Single-cell gene expression analysis of the human LAMM cells
 - Single-cell CAR-T_{reg} analysis from peripheral blood
 - Flow cytometry
 - Multiplex analysis of cytokines
 - Immunohistochemistry
 - Quantification of immunohistochemical staining
 - Immunofluorescence of murine samples
 - IMC image acquisition of tissue microarrays
 - IMC image preprocessing
 - Downstream analysis of human IMC data
 - Downstream analysis of murine IMC data
 - IMC distance analysis
 - Tissue processing for MICS
 - MICS image analysis
- **QUANTIFICATION AND STATISTICAL ANALYSIS**

SUPPLEMENTAL INFORMATION

Supplemental information can be found online at <https://doi.org/10.1016/j.ccell.2025.05.013>.

Received: August 25, 2024

Revised: March 23, 2025

Accepted: May 22, 2025

REFERENCES

1. Kamdar, M., Solomon, S.R., Arnason, J., Johnston, P.B., Glass, B., Bachanova, V., Ibrahim, S., Mielke, S., Mutsaers, P., Hernandez-Illizaliturri, F., et al. (2022). Lisocabtagene maraleucel versus standard of care with salvage chemotherapy followed by autologous stem cell transplantation as second-line treatment in patients with relapsed or refractory large B-cell lymphoma (TRANSFORM): results from an interim analysis of an open-label, randomised, phase 3 trial. *Lancet (London, England)* 399, 2294–2308. [https://doi.org/10.1016/S0140-6736\(22\)00662-6](https://doi.org/10.1016/S0140-6736(22)00662-6).
2. Locke, F.L., Miklos, D.B., Jacobson, C.A., Perales, M.-A., Kersten, M.-J., Oluwole, O.O., Ghobadi, A., Rapoport, A.P., McGuirk, J., Pagel, J.M., et al. (2022). Axicabtagene Ciloleucel as Second-Line Therapy for Large B-Cell Lymphoma. *N. Engl. J. Med.* 386, 640–654. <https://doi.org/10.1056/NEJMoa2116133>.
3. Neelapu, S.S., Jacobson, C.A., Ghobadi, A., Miklos, D.B., Lekakis, L.J., Oluwole, O.O., Lin, Y., Braunschweig, I., Hill, B.T., Timmerman, J.M., et al. (2023). Five-year follow-up of ZUMA-1 supports the curative potential of axicabtagene ciloleucel in refractory large B-cell lymphoma. *Blood* 141, 2307–2315. <https://doi.org/10.1182/blood.2022018893>.
4. Cappell, K.M., Sherry, R.M., Yang, J.C., Goff, S.L., Vanasse, D.A., McIntyre, L., Rosenberg, S.A., and Kochenderfer, J.N. (2020). Long-Term Follow-Up of Anti-CD19 Chimeric Antigen Receptor T-Cell Therapy. *J. Clin. Oncol.* 38, 3805–3815. <https://doi.org/10.1200/JCO.20.01467>.
5. Majzner, R.G., Rietberg, S.P., Sotillo, E., Dong, R., Vachharajani, V.T., Labanieh, L., Myklebust, J.H., Kadapakkam, M., Weber, E.W., Tousey, A.M., et al. (2020). Tuning the Antigen Density Requirement for CAR T-cell Activity. *Cancer Discov.* 10, 702–723. <https://doi.org/10.1158/2159-8290.CD-19-0945>.
6. Sotillo, E., Barrett, D.M., Black, K.L., Bagashev, A., Oldridge, D., Wu, G., Sussman, R., Lanauze, C., Ruella, M., Gazzara, M.R., et al. (2015). Convergence of Acquired Mutations and Alternative Splicing of CD19 Enables Resistance to CART-19 Immunotherapy. *Cancer Discov.* 5, 1282–1295. <https://doi.org/10.1158/2159-8290.CD-15-1020>.
7. Zhang, Z., Chen, X., Tian, Y., Li, F., Zhao, X., Liu, J., Yao, C., and Zhang, Y. (2020). Point mutation in CD19 facilitates immune escape of B cell lymphoma from CAR-T cell therapy. *J. Immunother. Cancer* 8, e001150. <https://doi.org/10.1136/jitc-2020-001150>.
8. Haradhvala, N.J., Leick, M.B., Maurer, K., Gohil, S.H., Larson, R.C., Yao, N., Gallagher, K.M.E., Katsis, K., Frigault, M.J., Southard, J., et al. (2022). Distinct cellular dynamics associated with response to CAR-T therapy for refractory B cell lymphoma. *Nat. Med.* 28, 1848–1859. <https://doi.org/10.1038/s41591-022-01959-0>.
9. Good, Z., Spiegel, J.Y., Sahaf, B., Malipatlolla, M.B., Ehlinger, Z.J., Kurra, S., Desai, M.H., Reynolds, W.D., Wong Lin, A., Vandris, P., et al. (2022). Post-infusion CAR TReg cells identify patients resistant to CD19-CAR therapy. *Nat. Med.* 28, 1860–1871. <https://doi.org/10.1038/s41591-022-01960-7>.
10. Jain, M.D., Zhao, H., Wang, X., Atkins, R., Menges, M., Reid, K., Spittler, K., Faramand, R., Bachmeier, C., Dean, E.A., et al. (2021). Tumor interferon signaling and suppressive myeloid cells are associated with CAR T-cell failure in large B-cell lymphoma. *Blood* 137, 2621–2633. <https://doi.org/10.1182/blood.2020007445>.
11. Majzner, R.G., and Mackall, C.L. (2018). Tumor Antigen Escape from CAR T-cell Therapy. *Cancer Discov.* 8, 1219–1226. <https://doi.org/10.1158/2159-8290.CD-18-0442>.
12. Scholler, N., Perbost, R., Locke, F.L., Jain, M.D., Turcan, S., Danan, C., Chang, E.C., Neelapu, S.S., Miklos, D.B., Jacobson, C.A., et al. (2022). Tumor immune contexture is a determinant of anti-CD19 CAR T cell efficacy in large B cell lymphoma. *Nat. Med.* 28, 1872–1882. <https://doi.org/10.1038/s41591-022-01916-x>.
13. Locke, F.L., Filosto, S., Chou, J., Vardhanabuthi, S., Perbost, R., Dreger, P., Hill, B.T., Lee, C., Zinzani, P.L., Kröger, N., et al. (2024). Impact of tumor microenvironment on efficacy of anti-CD19 CAR T cell therapy or chemotherapy and transplant in large B cell lymphoma. *Nat. Med.* 30, 507–518. <https://doi.org/10.1038/s41591-023-02754-1>.
14. Prima, V., Kaliberova, L.N., Kaliberov, S., Curiel, D.T., and Kusmartsev, S. (2017). COX2/mPGES1/PGE2 pathway regulates PD-L1 expression in tumor-associated macrophages and myeloid-derived suppressor cells. *Proc. Natl. Acad. Sci. USA* 114, 1117–1122. <https://doi.org/10.1073/pnas.1612920114>.
15. Ugel, S., De Sanctis, F., Mandruzzato, S., and Bronte, V. (2015). Tumor-induced myeloid deviation: when myeloid-derived suppressor cells meet tumor-associated macrophages. *J. Clin. Investig.* 125, 3365–3376. <https://doi.org/10.1172/JCI80006>.
16. Gabrilovich, D.I., Bronte, V., Chen, S.-H., Colombo, M.P., Ochoa, A., Ostrand-Rosenberg, S., and Schreiber, H. (2007). The terminology issue for myeloid-derived suppressor cells. *Cancer Res.* 67, 425–426. <https://doi.org/10.1158/0008-5472.CAN-06-3037>.
17. Bronte, V., Brandau, S., Chen, S.-H., Colombo, M.P., Frey, A.B., Greten, T.F., Mandruzzato, S., Murray, P.J., Ochoa, A., Ostrand-Rosenberg, S., et al. (2016). Recommendations for myeloid-derived suppressor cell nomenclature and characterization standards. *Nat. Commun.* 7, 12150. <https://doi.org/10.1038/ncomms12150>.
18. Veglia, F., Sanseviero, E., and Gabrilovich, D.I. (2021). Myeloid-derived suppressor cells in the era of increasing myeloid cell diversity. *Nat. Rev. Immunol.* 21, 485–498. <https://doi.org/10.1038/s41577-020-00490-y>.
19. Mantovani, A., Allavena, P., Marchesi, F., and Garlanda, C. (2022). Macrophages as tools and targets in cancer therapy. *Nat. Rev. Drug Discov.* 21, 799–820. <https://doi.org/10.1038/s41573-022-00520-5>.
20. Murga-Zamalloa, C., Rolland, D.C.M., Polk, A., Wolfe, A., Dewar, H., Chowdhury, P., Onder, O., Dewar, R., Brown, N.A., Bailey, N.G., et al. (2020). Colony-Stimulating Factor 1 Receptor (CSF1R) Activates AKT/mTOR Signaling and Promotes T-Cell Lymphoma Viability. *Clin. Cancer Res.* 26, 690–703. <https://doi.org/10.1158/1078-0432.CCR-19-1486>.
21. Manfroi, B., De Grandis, M., Moreaux, J., Tabruyn, S., Mayol, J.-F., Quintero, M., Righini, C., Sturm, N., Aurrand-Lions, M., and Huard, B. (2021). The microenvironment of DLBCL is characterized by noncanonical macrophages recruited by tumor-derived CCL5. *Blood Adv.* 5, 4338–4351. <https://doi.org/10.1182/bloodadvances.2021004203>.
22. Dean, E.A., Mhaskar, R.S., Lu, H., Mousa, M.S., Krivenko, G.S., Lazaryan, A., Bachmeier, C.A., Chavez, J.C., Nishihori, T., Davila, M.L., et al. (2020). High metabolic tumor volume is associated with decreased efficacy of axicabtagene ciloleucel in large B-cell lymphoma. *Blood Adv.* 4, 3268–3276. <https://doi.org/10.1182/bloodadvances.2020001900>.
23. Voltin, C.-A., Gödel, P., Beckmann, L., Heger, J.-M., Kobe, C., Kutsch, N., Borchmann, P., Dietlein, M., Herrmann, K., Stelljes, M., et al. (2023). Outcome Prediction in Patients With Large B-cell Lymphoma Undergoing Chimeric Antigen Receptor T-cell Therapy. *HemaSphere* 7, e817. <https://doi.org/10.1097/HS9.0000000000000817>.
24. Voltin, C.-A., Paccagnella, A., Winkelmann, M., Heger, J.-M., Casadei, B., Beckmann, L., Herrmann, K., Dekorsy, F.J., Kutsch, N., Borchmann, P., et al. (2024). Multicenter development of a PET-based risk assessment tool for product-specific outcome prediction in large B-cell lymphoma patients undergoing CAR T-cell therapy. *Eur. J. Nucl. Med. Mol. Imaging* 51, 1361–1370. <https://doi.org/10.1007/s00259-023-06554-0>.
25. Cassetta, L., and Pollard, J.W. (2018). Targeting macrophages: therapeutic approaches in cancer. *Nat. Rev. Drug Discov.* 17, 887–904. <https://doi.org/10.1038/nrd.2018.169>.
26. Al-Khami, A.A., Rodriguez, P.C., and Ochoa, A.C. (2016). Metabolic reprogramming of myeloid-derived suppressor cells (MDSC) in cancer. *Oncolimmunology* 5, e1200771. <https://doi.org/10.1080/2162402X.2016.1200771>.
27. Holtzhausen, A., Harris, W., Ubil, E., Hunter, D.M., Zhao, J., Zhang, Y., Zhang, D., Liu, Q., Wang, X., Graham, D.K., et al. (2019). TAM Family Receptor Kinase Inhibition Reverses MDSC-Mediated Suppression and Augments Anti-PD-1 Therapy in Melanoma. *Cancer Immunol. Res.* 7, 1672–1686. <https://doi.org/10.1158/2326-6066.CIR-19-0008>.

28. Li, F., and Ravetch, J.V. (2011). Inhibitory Fc γ receptor engagement drives adjuvant and anti-tumor activities of agonistic CD40 antibodies. *Science (New York, N.Y.)* 333, 1030–1034. <https://doi.org/10.1126/science.1206954>.
29. Ross, J.L., Chen, Z., Herting, C.J., Grabovska, Y., Szulzewsky, F., Puigdelloses, M., Monterroza, L., Switchenko, J., Wadhvani, N.R., Cimino, P.J., et al. (2021). Platelet-derived growth factor beta is a potent inflammatory driver in paediatric high-grade glioma. *Brain* 144, 53–69. <https://doi.org/10.1093/brain/awaa382>.
30. Guldner, I.H., Wang, Q., Yang, L., Golomb, S.M., Zhao, Z., Lopez, J.A., Brunory, A., Howe, E.N., Zhang, Y., Palakurthi, B., et al. (2020). CNS-Native Myeloid Cells Drive Immune Suppression in the Brain Metastatic Niche through Cxcl10. *Cell* 183, 1234–1248.e25. <https://doi.org/10.1016/j.cell.2020.09.064>.
31. Tu, S., Bhagat, G., Cui, G., Takaishi, S., Kurt-Jones, E.A., Rickman, B., Betz, K.S., Penz-Oesterreicher, M., Bjorkdahl, O., Fox, J.G., and Wang, T.C. (2008). Overexpression of interleukin-1beta induces gastric inflammation and cancer and mobilizes myeloid-derived suppressor cells in mice. *Cancer Cell* 14, 408–419. <https://doi.org/10.1016/j.ccr.2008.10.011>.
32. Lin, E.Y., Nguyen, A.V., Russell, R.G., and Pollard, J.W. (2001). Colony-stimulating factor 1 promotes progression of mammary tumors to malignancy. *J. Exp. Med.* 193, 727–740. <https://doi.org/10.1084/jem.193.6.727>.
33. Newman, A.M., Liu, C.L., Green, M.R., Gentles, A.J., Feng, W., Xu, Y., Hoang, C.D., Diehn, M., and Alizadeh, A.A. (2015). Robust enumeration of cell subsets from tissue expression profiles. *Nat. Methods* 12, 453–457. <https://doi.org/10.1038/nmeth.3337>.
34. Flümman, R., Hansen, J., Pelzer, B.W., Nieper, P., Lohmann, T., Kisis, I., Riet, T., Kohlhas, V., Nguyen, P.-H., Peifer, M., et al. (2023). Distinct Genetically Determined Origins of Myd88/BCL2-Driven Aggressive Lymphoma Rationalize Targeted Therapeutic Intervention Strategies. *Blood Cancer Discov.* 4, 78–97. <https://doi.org/10.1158/2643-3230.BCD-22-0007>.
35. Tabatabai, A., Arora, A., Höfmann, S., Jauch, M., von Tresckow, B., Hansen, J., Flümman, R., Jachimowicz, R.D., Klein, S., Reinhardt, H.C., and Knittel, G. (2023). Mouse models of diffuse large B cell lymphoma. *Front. Immunol.* 14, 1313371. <https://doi.org/10.3389/fimmu.2023.1313371>.
36. Flümman, R., Hansen, J., Meinel, J., Pfeiffer, P., Goldfarb Wittkopf, H., Lütz, A., Wirtz, J., Möllmann, M., Zhou, T., Tabatabai, A., et al. (2024). An inducible Cd79b mutation confers ibrutinib sensitivity in mouse models of Myd88-driven diffuse large B-cell lymphoma. *Blood Adv.* 8, 1063–1074. <https://doi.org/10.1182/bloodadvances.2023011213>.
37. Benner, B., Scarberry, L., Suarez-Kelly, L.P., Duggan, M.C., Campbell, A. R., Smith, E., Lapurga, G., Jiang, K., Butchar, J.P., Tridandapani, S., et al. (2019). Generation of monocyte-derived tumor-associated macrophages using tumor-conditioned media provides a novel method to study tumor-associated macrophages in vitro. *J. Immunother. Cancer* 7, 140. <https://doi.org/10.1186/s40425-019-0622-0>.
38. Elliott, L.A., Doherty, G.A., Sheahan, K., and Ryan, E.J. (2017). Human Tumor-Infiltrating Myeloid Cells: Phenotypic and Functional Diversity. *Front. Immunol.* 8, 86. <https://doi.org/10.3389/fimmu.2017.00086>.
39. Kinkhabwala, A., Herbel, C., Pankratz, J., Yushchenko, D.A., Rüberg, S., Praveen, P., Reiß, S., Rodriguez, F.C., Schäfer, D., Kollet, J., et al. (2022). MACSima imaging cyclic staining (MICS) technology reveals combinatorial target pairs for CAR T cell treatment of solid tumors. *Sci. Rep.* 12, 1911. <https://doi.org/10.1038/s41598-022-05841-4>.
40. Efreanova, M., Vento-Tormo, M., Teichmann, S.A., and Vento-Tormo, R. (2020). CellPhoneDB: inferring cell-cell communication from combined expression of multi-subunit ligand-receptor complexes. *Nat. Protoc.* 15, 1484–1506. <https://doi.org/10.1038/s41596-020-0292-x>.
41. Saito, T., Nishikawa, H., Wada, H., Nagano, Y., Sugiyama, D., Atarashi, K., Maeda, Y., Hamaguchi, M., Ohkura, N., Sato, E., et al. (2016). Two FOXP3(+)CD4(+) T cell subpopulations distinctly control the prognosis of colorectal cancers. *Nat. Med.* 22, 679–684. <https://doi.org/10.1038/nm.4086>.
42. Vandenberghe, K., van Gool, S.W., Kasran, A., Ceuppens, J.L., Boogaerts, M.A., and Vandenberghe, P. (1999). Interaction of CTLA-4 (CD152) with CD80 or CD86 inhibits human T-cell activation. *Immunology (Oxf.)* 98, 413–421. <https://doi.org/10.1046/j.1365-2567.1999.00888.x>.
43. Wing, K., Onishi, Y., Prieto-Martin, P., Yamaguchi, T., Miyara, M., Fehervari, Z., Nomura, T., and Sakaguchi, S. (2008). CTLA-4 control over Foxp3+ regulatory T cell function. *Science (New York, N.Y.)* 322, 271–275. <https://doi.org/10.1126/science.1160062>.
44. Roussel, M., Le, K.-S., Granier, C., Llamas Gutierrez, F., Foucher, E., Le Gallou, S., Pangault, C., Xerri, L., Launay, V., Lamy, T., et al. (2021). Functional characterization of PD1+TIM3+ tumor-infiltrating T cells in DLBCL and effects of PD1 or TIM3 blockade. *Blood Adv.* 5, 1816–1829. <https://doi.org/10.1182/bloodadvances.202003080>.
45. Morotti, M., Grimm, A.J., Hope, H.C., Arnaud, M., Desbuisson, M., Rayroux, N., Barras, D., Masid, M., Murgues, B., Chap, B.S., et al. (2024). PGE2 inhibits TIL expansion by disrupting IL-2 signalling and mitochondrial function. *Nature* 629, 426–434. <https://doi.org/10.1038/s41586-024-07352-w>.
46. Lacher, S.B., Dörr, J., de Almeida, G.P., Hönninger, J., Bayerl, F., Hirschberger, A., Pedde, A.-M., Meiser, P., Ramsauer, L., Rudolph, T. J., et al. (2024). PGE2 limits effector expansion of tumour-infiltrating stem-like CD8+ T cells. *Nature* 629, 417–425. <https://doi.org/10.1038/s41586-024-07254-x>.
47. Zhang, Y., Nicholatos, J., Dreier, J.R., Ricoult, S.J.H., Widenmaier, S. B., Hotamisligil, G.S., Kwiatkowski, D.J., and Manning, B.D. (2014). Coordinated regulation of protein synthesis and degradation by mTORC1. *Nature* 513, 440–443. <https://doi.org/10.1038/nature13492>.
48. Rogers, B.M., Smith, L., Dezzo, Z., Shi, X., DiGiammarino, E., Nguyen, D., Sethuraman, S., Zheng, P., Choi, D., Zhang, D., et al. (2021). VISTA is an activating receptor in human monocytes. *J. Exp. Med.* 218, e20201601. <https://doi.org/10.1084/jem.20201601>.
49. Tomolonis, J.A., Xu, X., Dholakia, K.H., Zhang, C., Guo, L., Courtney, A.N., Wang, S., Balzeau, J., Barragán, G.A., Tian, G., et al. (2023). Interaction between tumor cell TNFR2 and monocyte membrane-bound TNF- α triggers tumorigenic inflammation in neuroblastoma. *J. Immunother. Cancer* 11, e005478. <https://doi.org/10.1136/jitc-2022-005478>.
50. Chen, Z., Huang, A., Sun, J., Jiang, T., Qin, F.X.-F., and Wu, A. (2017). Inference of immune cell composition on the expression profiles of mouse tissue. *Sci. Rep.* 7, 40508. <https://doi.org/10.1038/srep40508>.
51. Dalton, H.J., Armaiz-Pena, G.N., Gonzalez-Villasana, V., Lopez-Berestein, G., Bar-Eli, M., and Sood, A.K. (2014). Monocyte subpopulations in angiogenesis. *Cancer Res.* 74, 1287–1293. <https://doi.org/10.1158/0008-5472.CAN-13-2825>.
52. Schmittnaegel, M., and De Palma, M. (2017). Reprogramming Tumor Blood Vessels for Enhancing Immunotherapy. *Trends Cancer* 3, 809–812. <https://doi.org/10.1016/j.trecan.2017.10.002>.
53. Morris, E.C., Neelapu, S.S., Giavridis, T., and Sadelain, M. (2022). Cytokine release syndrome and associated neurotoxicity in cancer immunotherapy. *Nat. Rev. Immunol.* 22, 85–96. <https://doi.org/10.1038/s41577-021-00547-6>.
54. Gust, J., Ponce, R., Liles, W.C., Garden, G.A., and Turtle, C.J. (2020). Cytokines in CAR T Cell-Associated Neurotoxicity. *Front. Immunol.* 11, 577027. <https://doi.org/10.3389/fimmu.2020.577027>.
55. Singh, N., Lee, Y.G., Shestova, O., Ravikumar, P., Hayer, K.E., Hong, S. J., Lu, X.M., Pajarillo, R., Agarwal, S., Kuramitsu, S., et al. (2020). Impaired Death Receptor Signaling in Leukemia Causes Antigen-Independent Resistance by Inducing CAR T-cell Dysfunction. *Cancer Discov.* 10, 552–567. <https://doi.org/10.1158/2159-8290.CD-19-0813>.
56. Lynn, R.C., Weber, E.W., Sotillo, E., Gennert, D., Xu, P., Good, Z., Anbunathan, H., Lattin, J., Jones, R., Tieu, V., et al. (2019). c-Jun overexpression in CAR T cells induces exhaustion resistance. *Nature* 576, 293–300. <https://doi.org/10.1038/s41586-019-1805-z>.
57. Heitzeneder, S., Bosse, K.R., Zhu, Z., Zhelev, D., Majzner, R.G., Radosevich, M.T., Dhingra, S., Sotillo, E., Buongervino, S., Pascual-Pasto, G., et al. (2022). GPC2-CAR T cells tuned for low antigen density

- mediate potent activity against neuroblastoma without toxicity. *Cancer Cell* 40, 53–69.e9. <https://doi.org/10.1016/j.ccell.2021.12.005>.
58. Stanley, E.R., and Chitu, V. (2014). CSF-1 receptor signaling in myeloid cells. *Cold Spring Harb. Perspect. Biol.* 6, a021857. <https://doi.org/10.1101/cshperspect.a021857>.
59. Pixley, F.J., and Stanley, E.R. (2004). CSF-1 regulation of the wandering macrophage: complexity in action. *Trends Cell Biol.* 14, 628–638. <https://doi.org/10.1016/j.tcb.2004.09.016>.
60. Talmadge, J.E., and Gabrilovich, D.I. (2013). History of myeloid-derived suppressor cells. *Nat. Rev. Cancer* 13, 739–752. <https://doi.org/10.1038/nrc3581>.
61. Valero, J.G., Matas-Céspedes, A., Arenas, F., Rodriguez, V., Carreras, J., Serrat, N., Guerrero-Hernández, M., Yahiaoui, A., Balagué, O., Martin, S., et al. (2021). The receptor of the colony-stimulating factor-1 (CSF-1R) is a novel prognostic factor and therapeutic target in follicular lymphoma. *Leukemia* 35, 2635–2649. <https://doi.org/10.1038/s41375-021-01201-9>.
62. Peranzoni, E., Lemoine, J., Vimeux, L., Feuillet, V., Barrin, S., Kantari-Mimoun, C., Bercovici, N., Guérin, M., Biton, J., Ouakrim, H., et al. (2018). Macrophages impede CD8 T cells from reaching tumor cells and limit the efficacy of anti-PD-1 treatment. *Proc. Natl. Acad. Sci. USA* 115, E4041–E4050. <https://doi.org/10.1073/pnas.1720948115>.
63. Haley, M.J., Bere, L., Minshull, J., Georgaka, S., Garcia-Martin, N., Howell, G., Coope, D.J., Roncaroli, F., King, A., Wedge, D.C., et al. (2024). Hypoxia coordinates the spatial landscape of myeloid cells within glioblastoma to affect survival. *Sci. Adv.* 10, ead33301. <https://doi.org/10.1126/sciadv.adj3301>.
64. Chiu, D.K.-C., Tse, A.P.-W., Xu, I.M.-J., Di Cui, J., Lai, R.K.-H., Li, L.L., Koh, H.-Y., Tsang, F.H.-C., Wei, L.L., Wong, C.-M., et al. (2017). Hypoxia inducible factor HIF-1 promotes myeloid-derived suppressor cells accumulation through ENTPD2/CD39L1 in hepatocellular carcinoma. *Nat. Commun.* 8, 517. <https://doi.org/10.1038/s41467-017-00530-7>.
65. Corzo, C.A., Condamine, T., Lu, L., Cotter, M.J., Youn, J.-I., Cheng, P., Cho, H.-I., Celis, E., Quiceno, D.G., Padhya, T., et al. (2010). HIF-1 α regulates function and differentiation of myeloid-derived suppressor cells in the tumor microenvironment. *J. Exp. Med.* 207, 2439–2453. <https://doi.org/10.1084/jem.20100587>.
66. Mulder, K., Patel, A.A., Kong, W.T., Piot, C., Halitzki, E., Dunsmore, G., Khalilnezhad, S., Irac, S.E., Dubuisson, A., Chevrier, M., et al. (2021). Cross-tissue single-cell landscape of human monocytes and macrophages in health and disease. *Immunity (Camb., Mass.)* 54, 1883–1900.e5. <https://doi.org/10.1016/j.immuni.2021.07.007>.
67. Zhu, Y., Knolhoff, B.L., Meyer, M.A., Nywening, T.M., West, B.L., Luo, J., Wang-Gillam, A., Goedegebuure, S.P., Linehan, D.C., and DeNardo, D.G. (2014). CSF1/CSF1R blockade reprograms tumor-infiltrating macrophages and improves response to T-cell checkpoint immunotherapy in pancreatic cancer models. *Cancer Res.* 74, 5057–5069. <https://doi.org/10.1158/0008-5472.CAN-13-3723>.
68. Sato, T., Sugiyama, D., Koseki, J., Kojima, Y., Hattori, S., Sone, K., Nishinakamura, H., Ishikawa, T., Ishikawa, Y., Kato, T., et al. (2025). Sustained inhibition of CSF1R signaling augments antitumor immunity through inhibiting tumor-associated macrophages. *JCI insight* 10, e178146. <https://doi.org/10.1172/jci.insight.178146>.
69. Gyori, D., Lim, E.L., Grant, F.M., Spensberger, D., Roychoudhuri, R., Shuttleworth, S.J., Okkenhaug, K., Stephens, L.R., and Hawkins, P.T. (2018). Compensation between CSF1R⁺ macrophages and Foxp3⁺ Treg cells drives resistance to tumor immunotherapy. *JCI insight* 3, e120631. <https://doi.org/10.1172/jci.insight.120631>.
70. Pyonteck, S.M., Akkari, L., Schuhmacher, A.J., Bowman, R.L., Sevenich, L., Quail, D.F., Olson, O.C., Quick, M.L., Huse, J.T., Teijeiro, V., et al. (2013). CSF-1R inhibition alters macrophage polarization and blocks glioma progression. *Nat. Med.* 19, 1264–1272. <https://doi.org/10.1038/nm.3337>.
71. Watson, S.S., Zomer, A., Fournier, N., Lourenco, J., Quadroni, M., Chryplewicz, A., Nassiri, S., Aubel, P., Avanthay, S., Croci, D., et al. (2024). Fibrotic response to anti-CSF-1R therapy potentiates glioblastoma recurrence. *Cancer Cell* 42, 1507–1527.e11. <https://doi.org/10.1016/j.ccell.2024.08.012>.
72. Li, W., Pan, L., Hong, W., Ginhoux, F., Zhang, X., Xiao, C., and Li, X. (2024). A single-cell pan-cancer analysis to show the variability of tumor-infiltrating myeloid cells in immune checkpoint blockade. *Nat. Commun.* 15, 6142. <https://doi.org/10.1038/s41467-024-50478-8>.
73. Fowler, N.H., Dickinson, M., Dreyling, M., Martinez-Lopez, J., Kolstad, A., Butler, J., Ghosh, M., Popplewell, L., Chavez, J.C., Bachy, E., et al. (2022). Tisagenlecleucel in adult relapsed or refractory follicular lymphoma: the phase 2 ELARA trial. *Nat. Med.* 28, 325–332. <https://doi.org/10.1038/s41591-021-01622-0>.
74. Wang, M., Munoz, J., Goy, A., Locke, F.L., Jacobson, C.A., Hill, B.T., Timmerman, J.M., Holmes, H., Jaglowski, S., Flinn, I.W., et al. (2020). KTE-X19 CAR T-Cell Therapy in Relapsed or Refractory Mantle-Cell Lymphoma. *N. Engl. J. Med.* 382, 1331–1342. <https://doi.org/10.1056/NEJMoa1914347>.
75. Vinnakota, J.M., Biavasco, F., Schwabenland, M., Chhatbar, C., Adams, R.C., Erny, D., Duquesne, S., El Khawanky, N., Schmidt, D., Fetsch, V., et al. (2024). Targeting TGF β -activated kinase-1 activation in microglia reduces CAR T immune effector cell-associated neurotoxicity syndrome. *Nat. Cancer* 5, 1227–1249. <https://doi.org/10.1038/s43018-024-00764-7>.
76. Tap, W.D., Gelderblom, H., Palmerini, E., Desai, J., Bauer, S., Blay, J.-Y., Alcindor, T., Ganjoo, K., Martin-Broto, J., Ryan, C.W., et al. (2019). Pexidartinib versus placebo for advanced tenosynovial giant cell tumour (ENLIVEN): a randomised phase 3 trial. *Lancet (London, England)* 394, 478–487. [https://doi.org/10.1016/S0140-6736\(19\)30764-0](https://doi.org/10.1016/S0140-6736(19)30764-0).
77. Monestime, S., and Lazaridis, D. (2020). Pexidartinib (TURALIO™): The First FDA-Indicated Systemic Treatment for Tenosynovial Giant Cell Tumor. *Drugs R&D* 20, 189–195. <https://doi.org/10.1007/s40268-020-00314-3>.
78. Cannarile, M.A., Weisser, M., Jacob, W., Jegg, A.-M., Ries, C.H., and Rüttinger, D. (2017). Colony-stimulating factor 1 receptor (CSF1R) inhibitors in cancer therapy. *J. Immunother. Cancer* 5, 53. <https://doi.org/10.1186/s40425-017-0257-y>.
79. Wolff, D., Cutler, C., Lee, S.J., Pusic, I., Bittencourt, H., White, J., Hamadani, M., Arai, S., Salhotra, A., Perez-Simon, J.A., et al. (2024). Axatilimab in Recurrent or Refractory Chronic Graft-versus-Host Disease. *N. Engl. J. Med.* 391, 1002–1014. <https://doi.org/10.1056/NEJMoa2401537>.
80. Dobin, A., Davis, C.A., Schlesinger, F., Drenkow, J., Zaleski, C., Jha, S., Batut, P., Chaisson, M., and Gingeras, T.R. (2013). STAR: ultrafast universal RNA-seq aligner. *Bioinformatics (Oxford, England)* 29, 15–21. <https://doi.org/10.1093/bioinformatics/bts635>.
81. Li, B., and Dewey, C.N. (2011). RSEM: accurate transcript quantification from RNA-Seq data with or without a reference genome. *BMC Bioinf.* 12, 323. <https://doi.org/10.1186/1471-2105-12-323>.
82. Love, M.I., Huber, W., and Anders, S. (2014). Moderated estimation of fold change and dispersion for RNA-seq data with DESeq2. *Genome Biol.* 15, 550. <https://doi.org/10.1186/s13059-014-0550-8>.
83. Ma, W., Kim, S., Chowdhury, S., Li, Z., Yang, M., Yoo, S., Petralia, F., Jacobsen, J., Li, J.J., Ge, X., et al. (2020). DreamAI: algorithm for the imputation of proteomics data. Preprint at bioRxiv. <https://doi.org/10.1101/2020.07.21.214205>.
84. Gu, Z. (2022). Complex heatmap visualization. *iMeta* 1, e43. <https://doi.org/10.1002/imt2.43>.
85. Wolf, F.A., Angerer, P., and Theis, F.J. (2018). SCANPY: large-scale single-cell gene expression data analysis. *Genome Biol.* 19, 15. <https://doi.org/10.1186/s13059-017-1382-0>.
86. Gayoso, A., Lopez, R., Xing, G., Boyeau, P., Valiollah Pour Amiri, V., Hong, J., Wu, K., Jayasuriya, M., Mehlman, E., Langevin, M., et al. (2022). A Python library for probabilistic analysis of single-cell omics data. *Nat. Biotechnol.* 40, 163–166. <https://doi.org/10.1038/s41587-021-01206-w>.

87. Bernstein, N.J., Fong, N.L., Lam, I., Roy, M.A., Hendrickson, D.G., and Kelley, D.R. (2020). Solo: Doublet Identification in Single-Cell RNA-Seq via Semi-Supervised Deep Learning. *Cell Syst.* *11*, 95–101.e5. <https://doi.org/10.1016/j.cels.2020.05.010>.
88. Levine, J.H., Simonds, E.F., Bendall, S.C., Davis, K.L., Amir, E.a.D., Tadmor, M.D., Litvin, O., Fienberg, H.G., Jager, A., Zunder, E.R., et al. (2015). Data-Driven Phenotypic Dissection of AML Reveals Progenitor-like Cells that Correlate with Prognosis. *Cell* *162*, 184–197. <https://doi.org/10.1016/j.cell.2015.05.047>.
89. McInnes, L., Healy, J., Saul, N., and Großberger, L. (2018). UMAP: Uniform Manifold Approximation and Projection. *JOSS* *3*, 861. <https://doi.org/10.21105/joss.00861>.
90. Hao, Y., Stuart, T., Kowalski, M.H., Choudhary, S., Hoffman, P., Hartman, A., Srivastava, A., Molla, G., Madad, S., Fernandez-Granda, C., and Satija, R. (2024). Dictionary learning for integrative, multimodal and scalable single-cell analysis. *Nat. Biotechnol.* *42*, 293–304. <https://doi.org/10.1038/s41587-023-01767-y>.
91. Troulé, K., Petryszak, R., Cakir, B., Cranley, J., Harasty, A., Prete, M., Tuong, Z.K., Teichmann, S.A., Garcia-Alonso, L., and Vento-Tormo, R. (2025). CellPhoneDB v5: inferring cell-cell communication from single-cell multiomics data. *Nat. Protoc.* <https://doi.org/10.1038/s41596-024-01137-1>.
92. La Manno, G., Soldatov, R., Zeisel, A., Braun, E., Hochgerner, H., Petukhov, V., Lidschreiber, K., Kastrioti, M.E., Lönnerberg, P., Furlan, A., et al. (2018). RNA velocity of single cells. *Nature* *560*, 494–498. <https://doi.org/10.1038/s41586-018-0414-6>.
93. Bergen, V., Lange, M., Peidli, S., Wolf, F.A., and Theis, F.J. (2020). Generalizing RNA velocity to transient cell states through dynamical modeling. *Nat. Biotechnol.* *38*, 1408–1414. <https://doi.org/10.1038/s41587-020-0591-3>.
94. Wolf, F.A., Hamey, F.K., Plass, M., Solana, J., Dahlin, J.S., Göttgens, B., Rajewsky, N., Simon, L., and Theis, F.J. (2019). PAGA: graph abstraction reconciles clustering with trajectory inference through a topology preserving map of single cells. *Genome Biol.* *20*, 59. <https://doi.org/10.1186/s13059-019-1663-x>.
95. Fang, Z., Liu, X., and Peltz, G. (2023). GSEAPy: a comprehensive package for performing gene set enrichment analysis in Python. *Bioinformatics (Oxford, England)* *39*, btac757. <https://doi.org/10.1093/bioinformatics/btac757>.
96. Badia-I-Mompel, P., Vélez Santiago, J., Braunger, J., Geiss, C., Dimitrov, D., Müller-Dott, S., Taus, P., Dugourd, A., Holland, C.H., Ramirez Flores, R.O., and Saez-Rodriguez, J. (2022). decoupleR: ensemble of computational methods to infer biological activities from omics data. *Bioinform. Adv.* *2*, vbac016. <https://doi.org/10.1093/bioadv/vbac016>.
97. Bankhead, P., Loughrey, M.B., Fernández, J.A., Dombrowski, Y., McArt, D. G., Dunne, P.D., McQuaid, S., Gray, R.T., Murray, L.J., Coleman, H.G., et al. (2017). QuPath: Open source software for digital pathology image analysis. *Sci. Rep.* *7*, 16878. <https://doi.org/10.1038/s41598-017-17204-5>.
98. Schindelin, J., Arganda-Carreras, I., Frise, E., Kaynig, V., Longair, M., Pietzsch, T., Preibisch, S., Rueden, C., Saalfeld, S., Schmid, B., et al. (2012). Fiji: an open-source platform for biological-image analysis. *Nat. Methods* *9*, 676–682. <https://doi.org/10.1038/nmeth.2019>.
99. Cheson, B.D., Fisher, R.I., Barrington, S.F., Cavalli, F., Schwartz, L.H., Zucca, E., Lister, T.A., Alliance, Australasian Leukaemia and Lymphoma Group, Eastern Cooperative Oncology Group, European Mantle Cell Lymphoma Consortium, et al. (2014). Recommendations for initial evaluation, staging, and response assessment of Hodgkin and non-Hodgkin lymphoma: the Lugano classification. *J. Clin. Oncol.* *32*, 3059–3068. <https://doi.org/10.1200/JCO.2013.54.8800>.
100. Budzies, J., Klauschen, F., Sinn, B.V., Györfy, B., Schmitt, W.D., Darb-Esfahani, S., and Denkert, C. (2012). Cutoff Finder: a comprehensive and straightforward Web application enabling rapid biomarker cutoff optimization. *PLoS One* *7*, e51862. <https://doi.org/10.1371/journal.pone.0051862>.
101. Li, M., Chiang, Y.-L., Lyssiotis, C.A., Teater, M.R., Hong, J.Y., Shen, H., Wang, L., Hu, J., Jing, H., Chen, Z., et al. (2019). Non-oncogene Addiction to SIRT3 Plays a Critical Role in Lymphomagenesis. *Cancer Cell* *35*, 916–931.e9. <https://doi.org/10.1016/j.ccell.2019.05.002>.
102. Flümman, R., Rehkämper, T., Nieper, P., Pfeiffer, P., Holzem, A., Klein, S., Bhatia, S., Kochanek, M., Kisis, I., Pelzer, B.W., et al. (2021). An Autochthonous Mouse Model of Myd88- and BCL2-Driven Diffuse Large B-cell Lymphoma Reveals Actionable Molecular Vulnerabilities. *Blood Cancer Discov.* *2*, 70–91. <https://doi.org/10.1158/2643-3230.BCD-19-0059>.
103. Gordon, S.R., Maute, R.L., Dulken, B.W., Hutter, G., George, B.M., McCracken, M.N., Gupta, R., Tsai, J.M., Sinha, R., Corey, D., et al. (2017). PD-1 expression by tumour-associated macrophages inhibits phagocytosis and tumour immunity. *Nature* *545*, 495–499. <https://doi.org/10.1038/nature22396>.
104. MacDonald, K.P.A., Palmer, J.S., Cronau, S., Seppanen, E., Olver, S., Raffelt, N.C., Kuns, R., Pettit, A.R., Clouston, A., Wainwright, B., et al. (2010). An antibody against the colony-stimulating factor 1 receptor depletes the resident subset of monocytes and tissue- and tumor-associated macrophages but does not inhibit inflammation. *Blood* *116*, 3955–3963. <https://doi.org/10.1182/blood-2010-02-266296>.
105. Prinz, L.F., Riet, T., Neureuther, D.F., Lennartz, S., Chrobok, D., Hübbe, H., Uhl, G., Riet, N., Hofmann, P., Hösel, M., et al. (2024). An anti-CD19/CTLA-4 switch improves efficacy and selectivity of CAR T cells targeting CD80/86-upregulated DLBCL. *Cell Rep. Med.* *5*, 101421. <https://doi.org/10.1016/j.xcrm.2024.101421>.
106. Cadilha, B.L., Benmebarek, M.-R., Dorman, K., Oner, A., Lorenzini, T., Obeck, H., Vääntinen, M., Di Pilato, M., Pruessmann, J.N., Stoiber, S., et al. (2021). Combined tumor-directed recruitment and protection from immune suppression enable CAR T cell efficacy in solid tumors. *Sci. Adv.* *7*, eabi5781. <https://doi.org/10.1126/sciadv.abi5781>.
107. Müller, N., Lorenz, C., Ostendorp, J., Heisel, F.S., Friese, U.P., Cartolano, M., Plenker, D., Tumbink, H., Heimsoeth, A., Baedeker, P., et al. (2023). Characterizing Evolutionary Dynamics Reveals Strategies to Exhaust the Spectrum of Subclonal Resistance in EGFR-Mutant Lung Cancer. *Cancer Res.* *83*, 2471–2479. <https://doi.org/10.1158/0008-5472.CAN-22-2605>.
108. Plubell, D.L., Wilmarth, P.A., Zhao, Y., Fenton, A.M., Minnier, J., Reddy, A. P., Klimek, J., Yang, X., David, L.L., and Pamir, N. (2017). Extended Multiplexing of Tandem Mass Tags (TMT) Labeling Reveals Age and High Fat Diet Specific Proteome Changes in Mouse Epididymal Adipose Tissue. *Mol. Cell. Proteomics* *16*, 873–890. <https://doi.org/10.1074/mcp.M116.065524>.
109. Subramanian, A., Tamayo, P., Mootha, V.K., Mukherjee, S., Ebert, B.L., Gillette, M.A., Paulovich, A., Pomeroy, S.L., Golub, T.R., Lander, E.S., and Mesirov, J.P. (2005). Gene set enrichment analysis: a knowledge-based approach for interpreting genome-wide expression profiles. *Proc. Natl. Acad. Sci. USA* *102*, 15545–15550. <https://doi.org/10.1073/pnas.0506580102>.
110. Schubert, M., Klinger, B., Klünemann, M., Sieber, A., Uhlitz, F., Sauer, S., Garnett, M.J., Blüthgen, N., and Saez-Rodriguez, J. (2018). Perturbation-response genes reveal signaling footprints in cancer gene expression. *Nat. Commun.* *9*, 20. <https://doi.org/10.1038/s41467-017-02391-6>.
111. vom Stein, A.F., Rebolledo-Rios, R., Lukas, A., Koch, M., von Lom, A., Reinartz, S., Bachurski, D., Rose, F., Bozek, K., Abdallah, A.T., et al. (2023). LYN kinase programs stromal fibroblasts to facilitate leukemic survival via regulation of c-JUN and THBS1. *Nat. Commun.* *14*, 1330. <https://doi.org/10.1038/s41467-023-36824-2>.
112. Ester, M., Kriegel, H.-P., Sander, J., and Xu, X. (1996). A Density-Based Algorithm for Discovering Clusters in Large Spatial Databases with Noise. In *Proceedings of 2nd International Conference (AAAI Press)*.

STAR★METHODS

KEY RESOURCES TABLE

REAGENT or RESOURCE	SOURCE	IDENTIFIER
Antibodies		
Mouse anti-human CD3 (clone OKT3)	BioLegend	Cat# 317347; RRID: AB_2571994
Mouse anti-human CD28 (clone 15E8)	In-house production	N/A
Rat anti-mouse CD3 (clone 17A2)	BioLegend	Cat# 100253; RRID: AB_2810314
Syrian hamster anti-mouse CD28 (clone 37.51)	BioLegend	Cat# 102121; RRID: AB_2810330
Rat anti-mouse CSF1R (clone AFS98)	BioXCell	Cat# BE0213; RRID: AB_2687699
Rabbit anti-phospho-AKT (Ser473)	Cell Signaling Technology	Cat# 9271; RRID: AB_329825
Rabbit anti-AKT	Cell Signaling Technology	Cat# 9272; RRID: AB_329827
Rabbit anti-phospho-p44/42 MAPK (Erk 1/2) (Thr202/Tyr204)	Cell Signaling Technology	Cat# 9101; RRID: AB_331646
Rabbit anti-p44/42 MAPK (Erk 1/2)	Cell Signaling Technology	Cat# 9102; RRID: AB_330744
Mouse anti-Actin (clone C4)	MP Biomedical	Cat# 08691001; RRID: AB_2335127
Goat anti-mouse IgG-HRP	Merck	Cat# 12-349; RRID: AB_390192
Goat anti-rabbit IgG-HRP	Merck	Cat# 12-348; RRID: AB_390191
Mouse anti-human CD3-BV605 (clone OKT3)	BioLegend	Cat# 317321; RRID: AB_11126166
Mouse anti-human CD3-APC (clone HIT3a)	BioLegend	Cat# 300312; RRID: AB_314048
Mouse anti-human CD20-AF700 (clone 2H7)	BioLegend	Cat# 302322; RRID: AB_493753
Mouse anti-human CD20-PE (clone 2H7)	BioLegend	Cat# 302306; RRID: AB_314254
Mouse anti-human CD4-BV510 (clone SK3)	BioLegend	Cat# 344634; RRID: AB_2566017
Mouse anti-human CD8-BUV737 (clone SK1)	BD Bioscience	Cat# 612755; RRID: AB_2870086
Mouse anti-human CD27-PE/Cy7 (clone M-T271)	BioLegend	Cat# 356412; RRID: AB_2562258
Mouse anti-human HLA-DR-BUV737 (clone L203)	BD Bioscience	Cat# 752496; RRID: AB_2917489
Mouse anti-human CD16-BUV805 (clone 3G8)	BD Bioscience	Cat# 748850; RRID: AB_2873253
Mouse anti-human CD11b-BV510 (clone ICRF44)	BioLegend	Cat# 301334; RRID: AB_2562112
Mouse anti-human CD45-BV570 (clone HI30)	BioLegend	Cat# 304034; RRID: AB_2563426
Mouse anti-human CD86-BV605 (clone IT2.2)	BioLegend	Cat# 305429; RRID: AB_11203889
Mouse anti-human CD163-BV785 (clone GHI/61)	BioLegend	Cat# 333632; RRID: AB_2728288
Mouse anti-human CD62L-FITC (clone DREG-56)	BioLegend	Cat# 304804; RRID: AB_314464
Mouse anti-human CD68-PerCP/Cyanine 5.5 (clone Y1/82A)	BioLegend	Cat# 333813; RRID: AB_10681723
Mouse anti-human CD80-PE (clone 2D10)	BioLegend	Cat# 305208; RRID: AB_314504
Mouse anti-human CD14-PE/Dazzle 594 (clone HCD14)	BioLegend	Cat# 325633; RRID: AB_2563624
Mouse anti-human PD-L1-PE/Cy7 (clone MIH3)	BioLegend	Cat# 374506; RRID: AB_2734434
Mouse anti-human CD15-APC (clone HI98)	BioLegend	Cat# 301907; RRID: AB_314199
Mouse anti-human CD33-Alexa700 (clone WM53)	BioLegend	Cat# 303435; RRID: AB_2810437
Mouse anti-human CD206-APC/Fire 750 (clone 15-2)	BioLegend	Cat# 321133; RRID: AB_2650956
Rat anti-human CSF1R-BV421 (clone 9-4D2-1E4)	BioLegend	Cat# 347321; RRID: AB_2687395
Rabbit anti-CSF1R (clone SP211)	Abcam	Cat# ab183316; RRID: AB_2885197
Rat anti-mouse B220 (clone RA3-6B2)	BD Bioscience	Cat# 550286; RRID: AB_393581
Rabbit anti-CD3 (clone SP7)	ThermoFisher	Cat# RM-9107-R7; RRID: AB_149921
Rabbit anti-mouse CSF1R-AF647 (clone EPR23529-26)	Abcam	Cat# ab275171
Goat anti-rabbit IgG-AF568	Abcam	Cat# ab175471; RRID: AB_2576207
Mouse anti-human CD3-APC (clone BW264/56)	Miltenyi	Cat# 130-113-125; RRID: AB_2725953
Anti-idiotypic CD19 CAR-Biotin	Miltenyi	Cat# 130-127-349; RRID: AB_2923109
Goat anti-mouse IgG Fab-Biotin	Southern Biotech	Cat# 1015-08; RRID: AB_2794195
Anti-Biotin-PE	Miltenyi	Cat# 130-110-951; RRID: AB_2661378
Goat anti-rat IgG Fab-Biotin	Jackson Immuno	Cat# 112-066-072; RRID: AB_2338185

(Continued on next page)

Continued

REAGENT or RESOURCE	SOURCE	IDENTIFIER
Armenian hamster anti-mouse CD3 ϵ -APC (clone: 145-2C11)	BioLegend	Cat# 100311; RRID: AB_312676
Rabbit anti-Histon H3 (clone D1H2)	Cell Signaling Technology	Cat# 60932; RRID: AB_3289584
Anti- aSMA-141Pr (clone 1A4)	Standard BioTools	Cat# 201508
Anti-human CD14-144Nd (clone EPR3653)	Standard BioTools	Cat# 3144025D; RRID: AB_2924314
Anti-human CD31-151Eu (clone EPR3094)	Standard BioTools	Cat# 3151025D; RRID: AB_2890140
Anti-CD68-159Tb (clone KP1)	Standard BioTools	Cat# 201508
Rabbit anti-CD79B (clone D7V2F)	Cell Signaling Technology	Cat# 96024; RRID: AB_2800254
Anti-CD8a-162Dy (clone C8/144B)	Standard BioTools	Cat# 201508
Rabbit anti-human CD79A (clone D1X5C)	Cell Signaling Technology	Cat# 13333; RRID: AB_2798183
Anti-CD3-170Er (polyclonal, C-terminal)	Standard BioTools	Cat# 201508
Rabbit anti-mouse CD45 (clone D3F8Q)	Cell Signaling Technology	Cat# 98819
Rabbit anti-CD31 (clone EPR17259)	Abcam	Cat# ab225883; RRID: AB_2943140
Rabbit anti-mouse CD8 alpha (clone EPR21769)	Abcam	Cat# ab230156
Rabbit anti-mouse CD4 (clone BLR167J)	Bethyl	Cat# A700-167; RRID: AB_2891959
Rabbit anti-CD11b (clone EPR1344)	Abcam	Cat# ab216445; RRID: AB_2864378
Rabbit anti-mouse F4/80 (clone D2S9R)	Cell Signaling Technology	Cat# 25514
Anti-Collagen type 1-169Tm (polyclonal)	Standard BioTools	Cat# 201508
Rat anti-mouse B220 (CD45R) (clone RA3-6B2)	BD Bioscience	Cat# 557390; RRID: AB_396673
Biological samples		
Primary human lymphoma specimens	University Hospital Cologne	N/A
Chemicals, peptides, and recombinant proteins		
Pancoll human	PanBiotech	Cat#P04-601000
Human AB-Serum	Sigma-Aldrich	Cat#4522
Recombinant human IL-4	ImmunoTools	Cat#11340047
Recombinant human IL-10	ImmunoTools	Cat#11340107
Recombinant human M-CSF	ImmunoTools	Cat#11343117
BLZ-945	Selleckchem	Cat#S7725
Lymphoprep	Stemcell Technologies	Ca#18060
Recombinant human IL-2 (Proleukin S)	Clinigen	N/A
Recombinant human IL-15	ImmunoTools	Cat#11340155
Human TruStain FcX	BioLegend	Cat#422302
ProLong Gold Antifade Mountant	Thermofisher	Cat#P36934
165Ho metalated DTPA-diTy	Nicole Potter, Mark Nitz	N/A
Intercalator-Ir solution	Standard BioTools	Cat#201192B
MACSima Running Buffer	Miltenyi	Cat#130-121-565
Zombie UV Viability dye	BioLegend	Cat#423108
Zombie NIR Viability dye	BioLegend	Cat#423106
Streptavidin-PE	BioLegend	Cat#405203
Cell lysis buffer	Cell Signaling Technology	Cat#9803S
Phosphatase inhibitor cocktail 2	Sigma-Aldrich	Cat#P5726
Protease inhibitor cocktail tablets	Sigma-Aldrich	Cat#11836170001
4xNuPage LDS buffer	Thermofisher	Cat#NP0007
NuPage sample reducing agent	Thermofisher	Cat#NP0009
Bolt Bis-Tris Gels 4-12%	Thermofisher	Cat#NW04122BOX
Milk powder	Carl Roth	Cat#T145.2
Lys-C	Wako/Fujifilm	Cat#125-05061
Critical commercial assays		
Maxwell RSC RNA FFPE Kit	Promega	Cat#AS1440
RNeasy Mini Kit	Qiagen	Cat#74104

(Continued on next page)

Continued

REAGENT or RESOURCE	SOURCE	IDENTIFIER
BCA Protein Assay	ThermoFisher	Cat#23225
Tyramide superboost kit	ThermoFisher	Cat#B40944
MojoSort Mouse CD3 T cell Isolation Kit	BioLegend	Cat#480031
EasySep Human Monocyte Enrichment Kit	Stemcell Technologies	Cat#19059
660 nm assay kit	ThermoFisher	Cat#22663
Fluorometric peptide assay	ThermoFisher	Cat#23290

Deposited data

Bulk RNA-seq data from human B-NHL specimens (<i>n</i> = 24)	This paper	Zenodo: https://doi.org/10.5281/zenodo.15280550
Single-cell RNA-seq data from human B-NHL specimens (<i>n</i> = 7)	This paper	Zenodo: https://doi.org/10.5281/zenodo.15280550
Proteomic data of human monocytes and <i>ex vivo</i> generated human LAMM cells	This paper	Zenodo: https://doi.org/10.5281/zenodo.15280550

Experimental models: Cell lines

Human: HEK 293T cells	DSMZ	Cat#ACC635
Human: SU-DHL-4	Ruth Flümman	N/A
Human: RIVA	Ruth Flümman	N/A

Experimental models: Organisms/strains

Mouse: C57BL/6 wild-type	In-house breeding	N/A
Mouse: <i>Prdm1</i> ^{fl/fl} ; <i>Myd88</i> ^{cond.p.L252P/wt} ; <i>Rosa26</i> ^{LSL.BCL2.IRES.GFP/wt} ; <i>Cd19</i> ^{Cre/wt} (PPMBC)	Ruth Flümman, Gero Knittel, Hans Christian Reinhardt	N/A

Recombinant DNA

Plasmid: pBullet_aCD19_4-1BB_CD3zeta (human)	Tobias Riet, Markus Chmielewski	N/A
Plasmid: RSF91_aCD19_CD28_CD3zeta_P2A_eGFP (mouse)	Tobias Riet, Markus Chmielewski	N/A

Software and algorithms

R package FastQC (v0.11.4)	N/A	N/A
R package STAR aligner (v2.7.0)	Dobin et al. ⁸⁰	N/A
R package RSEM (v1.3.1)	Li et al. ⁸¹	N/A
DESeq2	Love et al. ⁸²	N/A
GSEA software (v4.3.2)	Broad Institute	N/A
CIBERSORTx	Newman et al. ³³	N/A
LM22	Newman et al. ³³	N/A
ImmuCC	Chen et al. ⁵⁰	N/A
Proteome Discoverer (v3.1.1.93)	ThermoFisher	N/A
DreamAI	Ma et al. ⁸³	N/A
R package ComplexHeatmap	Gu ⁸⁴	N/A
Python package scanpy (v1.9.6 and v1.10.3)	Wolf et al. ⁸⁵	N/A
Scvi-tools (v1.0.4)	Gayoso et al. ⁸⁶	N/A
SOLO (through the scvi-tools)	Bernstein et al. ⁸⁷	N/A
PhenoGraph (through the scanpy package)	Levine et al. ⁸⁸	N/A
UMAP (through the scanpy package)	McInnes et al. ⁸⁹	N/A
R package Seurat (v5.0.0)	Hao et al. ⁹⁰	N/A
CellPhoneDB (v5)	Troulé et al. ⁹¹	N/A
R package ktplots (v2.4.2)	Troulé et al. ⁹¹	N/A
R package velocyto (v0.17.17)	La Manno et al. ⁹²	N/A
Python package scvelo (v0.3.3)	Bergen et al. ⁹³	N/A
PAGA (through the scvelo package)	Wolf et al. ⁹⁴	N/A
Python package gseapy (v1.1.1)	Fang et al. ⁹⁵	N/A
Python package decoupler (v1.9.2)	Badia-I-Mompel et al. ⁹⁶	N/A

(Continued on next page)

Continued

REAGENT or RESOURCE	SOURCE	IDENTIFIER
QuPath (v0.50)	Bankhead et al. ⁹⁷	N/A
Fiji (v1.54f)	Schindelin et al. ⁹⁸	N/A
MACS iQ View Software (v1.3.1)	Miltenyi	N/A
FlowJo	FlowJo LLC	N/A
Python package scikit-image (v0.18.1)	N/A	N/A
Python package scipy.ndimage (v10.1)	N/A	N/A
Python package scikit-learn (v1.3.2)	N/A	N/A
Python package open-cv (v4.2.0.32)	N/A	N/A
Python package numpy (v1.22.4)	N/A	N/A
BioRender	Science Suite Inc.	N/A
SPSS (v29.0.0.0)	IBM	N/A
Prism	Graph Pad	N/A
Excel 2021	Microsoft	N/A
Word 2021	Microsoft	N/A
Inkscape (v0.92.4)	Inkscape Community	N/A

EXPERIMENTAL MODEL AND STUDY PARTICIPANT DETAILS

Patient cohorts and samples

Patients with r/r aggressive B-NHL treated with CAR-T cells at the University Hospital Cologne were eligible for this study ($n = 106$). Patients provided informed consent for research using their lymphoma samples and de-identified health information as a part of the BioMaSOTA (Biologische Material Sammlung zur Optimierung Therapeutischer Ansätze) protocol that was approved by the Ethics Committee of the University of Cologne. Clinical data were obtained retrospectively from chart review (Table S1). Treatment response was assessed radiographically according to the Lugano criteria.⁹⁹ Formalin-fixed and paraffin-embedded (FFPE) lymphoma specimens were retrieved from the archives of the Institute of Pathology at the University Hospital Cologne. For preparation of single-cell suspensions, lymphoma tissue was processed immediately after biopsy or surgery. In brief, tissue was cut into small pieces, collected in PBS and then filtered through a 100 μm strainer into a sterile 50 mL conical tube. The cell suspension was washed with PBS twice (300g / 1400rpm / 5 min) at 4°C and the supernatant was discarded. Afterwards, cells were resuspended in freezing medium (90% FBS, 10% DMSO; max. 5×10^7 cells per mL) and stored in liquid nitrogen until use. Specimens taken within six months before CAR-T cell therapy were used for downstream analyses of clinical data. DR was defined as complete remission six months after CAR-T cell infusion. Two DR patients of the experimental cohort received radiation therapy within six months post-CAR-T cell therapy and were therefore excluded from downstream evaluation as indicated in Figure 1C and Table S1. To identify biologically relevant prognostic patient subgroups and determine the optimal cutoff for survival analyses, we applied percentile-based thresholds (Figures 1D, 2H, and S3) or the Cutoff Finder tool (Figures 2C and 2D).^{100,101}

Cell lines

Human SU-DHL4 and RIVA cell lines were maintained in RPMI medium with 20% FBS. To obtain lymphoma-conditioned media, cells were plated at a concentration of 1×10^6 cells/mL in RPMI supplemented with 0.2% FBS. 24 h later media was harvested, centrifuged and filtered (40 μm). Media was frozen after the addition of 10% FBS.

Experimental mice

Lymphoma-bearing C57BL/6 PPMBC mice whose generation has been described previously³⁴ were used for *in vivo* experiments. Monitoring of lymphoma burden was assessed using mouse MRI as described earlier.¹⁰² In treatment studies, PPMBC mice were separated into low and high tumor volume groups based on spleen size detectable by MRI. High tumor volume was defined by splenomegaly larger than 400 μL , with a robust volume increase in two consecutive scans, if not otherwise indicated. For anti-CD19 CAR-T cell experiments, 2×10^6 engineered murine CAR-T cells were intravenously injected into mice on day 0. *In vivo* CSF1R blockade was performed by using an anti-CSF1R antibody (clone AFS98) which was purchased from BioXCell and dissolved in PBS. Mice were treated three times per week with 400 μg of antibody per dose via intraperitoneal injection as per Gorden et al.¹⁰³ and MacDonald et al.¹⁰⁴ (16 mg/kg body weight). Treatment was started at day -2 until day 28 post-CAR-T cell infusion. Lymphoma response was subsequently monitored by weekly MRI and PFS and OS were recorded. For survival analyses, animals were recorded as events if they succumbed to disease or had to be sacrificed due to predefined termination criteria. Animals that died due to disease-unrelated reasons (appendicitis, abnormal teeth, injuries inflicted by cage mates) were censored. To assess CAR-T cell expansion, blood was collected from the facial vein into heparin and plasma tubes. To obtain tissue samples, mice were euthanized by

cervical dislocation, and spleens as well as visible lymph nodes were extracted. Samples were either formalin-fixed and paraffin-embedded, or flash-frozen. Alternatively, extracted tissue specimens were mashed, strained (40 μ m) and incubated with red blood cell lysis buffer to generate single-cell suspensions. Freezing medium (90% FBS, 10% DMSO; max. 5x10⁷ cells per mL) was added to the cells for storage at -80°C prior to analyses. All animal experiments were approved by the Landesamt für Natur, Umwelt und Verbraucherschutz Nordrhein-Westfalen (LANUV) (2022.A146).

METHOD DETAILS

Quantitative PET analysis

Two expert readers performed MTV measurements semi-automatically with a standardized uptake value of 4.0 using the ACCURATE tool (PETRA consortium, Amsterdam, The Netherlands) and syngo.via (Siemens Healthcare GmbH, Erlangen, Germany) as described previously.^{23,24} In lymphoma tissue surrounded by areas of high physiological uptake, such as central nervous system lesions, manual correction was needed to avoid overestimating the tumor volume.

Cell culture

Peripheral blood mononuclear cells (PBMCs) were isolated from healthy donor buffy coats (Transfusion Medicine, University Hospital Cologne) as follows. First, whole blood was diluted in PBS (1:1). The PBMC layer was then recovered through density gradient centrifugation (800g, 20 min, Acc: 6, Dec: 1) using Pancoll Human (PanBiotech). PBMCs were washed twice with PBS and remaining erythrocytes were lysed using red blood cell lysis buffer. Monocytes were isolated from healthy donor PBMCs utilizing the EasySep Human Monocyte Enrichment Kit (Stemcell Technologies) according to the manufacturer's instructions resulting in highly pure populations of enriched CD11b⁺/CD14⁺ monocytes. For differentiation of *ex vivo* generated human CSF1R⁺CD14⁺CD68⁺ LAMM cells we followed a recently established protocol.³⁷ Here we cultivated cells in equal volumes of lymphoma-conditioned media and HAB media (RPMI + 10% human AB-Serum + L-Glutamin + 1% Penicillin/Streptomycin) supplemented with 1 μ g/mL of rhIL-4, rhIL-10 and rhM-CSF (all ImmunoTools). 2x10⁶ enriched monocytes were plated per well of a 6-well plate at a concentration of 1.33x10⁶ cells/mL. Afterwards, media was changed every 24 h until day 7, when cells were harvested for co-culture experiments. No additional downstream enrichment was performed as *ex vivo* generated human LAMM cells were already highly positive for CSF1R, CD14 and CD68 and to avoid cellular stress. For co-culture assays CAR-T cells were generated from matched donors and cells were plated in 96-well plates at a concentration of 50,000 cells/well. For *in vitro* CSF1R inhibition we used the CSF1R inhibitor BLZ-945 (600nM) (Selleckchem) for 24h.

Human and murine anti-CD19 CAR-T cells

Human T cells were derived from healthy donor PBMCs. The usage has been consented by donors and approved by the ethics committee of the University of Cologne. PBMCs were isolated via gradient centrifugation with Lymphoprep (Stemcell Technologies), and T cells were activated with 1000 U/mL rhIL-2 (Proleukin S) (Clinigen), 200 ng/mL anti-CD3 (clone OKT3) (BioLegend) and 50 ng/mL anti-CD28 (clone 15E8) (in-house production) in RPMI supplemented with 10% FBS. Two days post activation T cells were transduced on plates coated with poly-D-Lysin, which were centrifuged at 800g for 90 min and cultured overnight with viral supernatant as described previously.¹⁰⁵ The following day, transduction was repeated. Here, T cells were kept stimulated overnight with 1000 U/mL of rhIL-2. For human CAR-T cells, we utilized human anti-CD19 CAR vector DNA co-transfected with VSVg envelope and MoMuLV gag/pol plasmids as described previously.¹⁰⁵

Dual knock-out of the PGE₂ receptors EP2/EP4 via CRISPR/Cas9 editing in cells was performed on the day of T cell isolation, as previously described.¹⁰⁶ In short, two different Alt-R CRISPR-Cas9 crRNAs (IDT) for each of the receptors EP2 and EP4 were hybridized with Alt-R CRISPR-Cas9 tracrRNA (100 μ M, IDT). RNPs were formed with Alt-R Cas9 Electroporation Enhancer and Alt-R S.p. Cas9 Nuclease V3. T cells and RNPs were resuspended in 100 μ L in electroporation buffer P3 (Lonza) in a Nucleocuvette Vessel (Lonza), whereafter nucleofection was performed in a 4D Nucleofector (Lonza) with the pulse program EH115 (human T cells).

For generation of murine anti-CD19 CAR-T cells, T cells were isolated from spleens of C57BL/6 wild-type mice using the MojoSort Mouse CD3 T cell Isolation Kit (BioLegend). Murine T cells were stimulated with 200 ng/mL anti-CD3 (BioLegend), 100ng/mL anti-CD28 (BioLegend), 1000 U/mL rhIL-2 (Proleukin S) (Clinigen) and 10 ng/mL rhIL-15 (ImmunoTools). Viral supernatant was centrifuged onto 6-well plates coated with poly-D-Lysin at 800g for 90 min after which the cells were added and centrifuged again at 300g for 10 min. For transduction experiments, murine T cells were cultured in RPMI media supplemented with 10% FBS, Penicillin/Streptomycin, HEPES buffer, 1% Sodium-pyruvate, 1% MEM NEAA, 0.1% β -Mercaptoethanol, 1000 U/mL rhIL-2 (Proleukin S) (Clinigen) and 10 ng/mL rhIL-15 (ImmunoTools). Retrovirus for transduction of murine T cells was produced by HEK 293T cells co-transfected with the same helper plasmid coding genes (VSVg-env, MLV gag/pol) together with the anti-CD19 CAR as described previously.³⁴

Bulk RNA-seq of human and murine samples

Human specimens collected from CAR-T cell-treated patients at the University Hospital Cologne were archived at the Institute of Pathology. RNA was extracted from FFPE tissue samples using the Maxwell RSC RNA FFPE Kit on the Maxwell RSC (Promega) according to the manufacturer's instructions.

RNA from human healthy monocytes and *ex vivo* generated human LAMM cells were isolated using the RNeasy Mini Kit (Qiagen) according to the manufacturer's instructions.

Previously flash-frozen murine spleens from PPMBC mice were thawed quickly, and 20–30 μg of tissue were used as starting material for RNA isolation utilizing the RNeasy Mini Kit (Qiagen). Samples were eluted in 30–50 μL of RNase-free water and stored at –80 °C. Library preparation and bulk 3' RNA-seq were performed at the Cologne Center for Genomics (CCG) (Cologne, Germany) according to their standard protocols. Libraries for RNA-seq were generated using the QuantSeq 3' mRNA-seq library kit (Lexogen) and following the manufacturer's instructions. The KAPA Library Quantification kit (Peqlab) and the 7900HT Sequence Detection System (Applied Biosystems) were used to quantify pools. Single-read (1x50bp) sequencing was performed on the Illumina HiSeq4000.

Bulk RNA analysis of human and murine samples

Bulk RNA-seq data were processed using our established pipeline.¹⁰⁷ In brief, quality of FASTQ files of 3' UTR RNA-seq were checked using FastQC (v0.11.4). Reads were mapped to the human reference genome GRCh38 or mouse reference genome GRCm38 (p6), respectively, using the STAR aligner (v2.7.0). Prior to downstream analysis, expression was quantified with RSEM (v1.3.1). Data were normalized, and statistics were calculated using DESeq2. These analyses were carried out on the computing cluster of the Regional Computing Centre of the University of Cologne (RRZK) (Cologne, Germany). GSEA was performed using GSEA software (v4.3.2). Counts per million (CPM) were used as input. Compared groups are indicated within each figure and corresponding figure legend. Analyses were run with 1000 permutations, excluding gene sets smaller than five genes. Otherwise, standard settings were applied. *In silico* cytometry was conducted using CIBERSORTx³³ analyses. This algorithm allows deconvolution of bulk RNA-seq data to estimate the relative fraction of infiltrating immune cells using a signature matrix. For the human and mouse samples we used the LM22³³ and ImmuCC⁵⁰ signature matrices, respectively. Batch correction (B-mode) and 1000 permutations were applied (other parameters were left at default values). LAMM relevant genes were identified from literature search. To calculate the combined Bulk-LAMM signature z-score within tumor samples, we calculated the mean of row z-scores from individual LAMM genes. Similarly, the combined M2-related mouse gene signature was calculated based on the following genes: *Mrc1*, *Tgm2*, *Retnla*, *Arg1*, *Ccl22*, *Cd163*.

Global protein profiling

For proteome profiling, cell pellets from human healthy donor monocytes and *ex vivo* generated human CSF1R⁺CD14⁺CD68⁺ LAMM cells were lysed in urea lysis buffer (8 M urea, 20 mM HEPES, pH 8.0, 1 mM sodium orthovanadate, 2.5 mM sodium pyrophosphate, 1 mM beta-glycerophosphate). Protein concentrations of the lysates were determined using the 660 nm assay kit (ThermoFisher) according to the manufacturer's instructions. 60 μg of protein per sample were reduced with DTT (10 mM for 1 h at 37 °C), alkylated with iodoacetamide (25 mM for 15 min at 37 °C in the dark) and digested using Lys-C (Wako/Fujifilm) for 2 h at 37 °C in an enzyme-to-substrate ratio of 1:50 (w/w). After dilution with 20 mM HEPES (pH 8.0) to a concentration of 2 M urea, digestion was continued overnight with trypsin at 37 °C and 1:50 (w/w) enzyme-to-substrate ratio. The peptide mixtures were acidified, purified using C18 spin tips and dried by vacuum centrifugation. Afterwards, the peptide samples were dissolved in 0.1 % formic acid and peptide concentrations were determined using a fluorometric peptide assay (ThermoFisher). The peptide samples were analyzed by LC-MS/MS on a Vanquish Neo UHPLC system (ThermoFisher) coupled online to an Orbitrap Astral mass spectrometer (ThermoFisher) in a data-independent acquisition scheme (DIA). 400 ng of peptides from each sample were concentrated and desalted on a PepMap Neo trap cartridge (ThermoFisher, particle size 100 Å, inner diameter 300 μm, length 5 mm), followed by separation on a 50 cm μPAC C18 analytical column (ThermoFisher) using a 22 min method (18 min linear gradient) of 1% to 28% acetonitrile in 0.1% formic acid at a flow rate of 250 nL/min. Precursor ion survey scans were acquired using the Orbitrap mass analyzer with the following parameters: resolution 240,000, scan range m/z 380–980, automatic gain control (AGC) target 5x10⁶, maximum injection time 10 ms, RF lens setting 40%. For fragment ion scans using the Astral mass analyzer, precursor ions were isolated for collision-induced dissociation (HCD) through each survey scan with an isolation window of m/z 2, resulting in 299 scan events. The normalized HCD collision energy was set to 25% and for fragment ion analysis the AGC target was 5x10⁴ at a maximum injection time of 3 ms.

Global protein analysis

Raw DIA data were analyzed using Proteome Discoverer (v3.1.1.93) (ThermoFisher). Spectra were searched against the Uniprot human reference proteome and 245 frequently observed contaminants using the CHIMERYS search algorithm. The mass tolerance for fragment ions was set to 10 ppm. Oxidation of methionine was considered as dynamic modification while carbamidomethylation of cysteine was defined as a fixed modification. The peptide length was defined to be between seven to 30 amino acids with one allowed missed cleavage site. One to four charges per peptide were allowed. At both peptide and protein level, the false discovery rate (FDR) was set at 1%. Further data processing was done using R studio. First, contaminants were removed. To control for equal sample loading, intensities from each LC-MS/MS run were normalized on the median of the summed-up intensities from each sample.¹⁰⁸ Finally, data were filtered for proteins found in at least 70% of the samples. The remaining missing values were imputed using the DreamAI algorithm in R.⁸³ Protein intensities were z-score normalized on a per-protein basis by subtracting the mean intensity and dividing by the standard deviation. The Euclidean distance was then calculated from these z-scored values for hierarchical clustering and the resulting heatmap was generated using the ComplexHeatmap package in R.⁸⁴

Western blot

Human healthy donor monocytes and *ex vivo* generated human CSF1R⁺CD14⁺CD68⁺ LAMM cells were washed in PBS and lysed in cell lysis buffer (Cell Signaling Technology) containing phosphatase (Sigma-Aldrich) and protease (Sigma-Aldrich) inhibitors. The BCA Protein Assay (ThermoFisher) was used to determine protein concentrations. To separate the protein samples via SDS-PAGE, the cell lysates were incubated with 4xNuPage LDS buffer (ThermoFisher) and sample reducing agent (10x) (ThermoFisher) for 10 min at 80°C. The samples were loaded onto Bolt Bis-Tris Gels 4–12 % (ThermoFisher). Protein transfer to a nitrocellulose membrane (Amersham) was performed by wet blotting. To perform immunodetection, membranes were blocked with 4% (w/v) milk powder (Carl Roth) diluted in TBS with Tween 0.05 % (TBS-T; pH 7.6), incubated with primary antibodies using anti-phospho-AKT (Ser473), anti-AKT, anti-phospho-p44/42 MAPK (Erk 1/2) (Thr202/Tyr204), anti-p44/42 MAPK (Erk 1/2) (all Cell Signaling Technology), anti-Actin (MP Biomedical) and HRP-coupled anti-mouse (Merck) / rabbit (Merck) secondary antibodies were used. Immunodetection was performed using ECL Western Blot Detection Reagent (Amersham) and ECL Hyperfilm (Amersham).

Droplet-based scRNA-seq of human and murine samples

For scRNA-seq studies of human samples we analyzed primary B-NHL tissue samples of seven patients with *r/r* disease eligible for CAR-T cell therapy using Chromium Single Cell 5'v2 V(D)J technology (10X Genomics). For all specimens, *r/r* disease was independently confirmed by board-certified pathologists. For scRNA-seq studies of murine samples we analyzed diseased spleens of four C57BL/6 PPMBC mice using Chromium Single Cell 5'v3 V(D)J technology (10X Genomics). Single-cell suspensions were processed by using the 10X Genomics Chromium X following the protocol described in the Chromium Single Cell V(D)J Reagent Kits User Guide. Chromium Next GEM Single Cell 5' Library was applied during the process. Oil droplets of encapsulated single cells and barcoded beads (GEMs) were subsequently reverse-transcribed resulting in cDNA tagged with a cell barcode and unique molecular index (UMI). Next, cDNA was amplified to generate single-cell libraries according to the manufacturer's protocol. Amplified full-length cDNA from poly-adenylated mRNA was used to amplify full-length V(D)J segments (10x Barcoded) via PCR amplification with primers specific to either the TCR or BCR constant regions. As both T and B cells were expected to be present in the partitioned cell population, TCR and Ig transcripts could be amplified in separate reactions from the same amplified cDNA material. Afterwards, amplified cDNA was enzymatically fragmented, end-repaired and polyA tagged. Next, Illumina sequencing adapters were ligated to the size-selected fragments. Finally, sample indices were selected and amplified, followed by a double-sided size selection. Samples were then sequenced on an Illumina NovaSeq 6000 as paired-end mode.

Single-cell data pre-processing

For single-cell data pre-processing, the Scanpy (v1.9.6) Python package⁸⁵, a scalable toolkit tailored for the analysis of single-cell data, was used to perform quality control, ensuring the inclusion of cells with over 150 genes. Following best practices, we employed ratios instead of hard thresholds, allowing cutoffs to adapt to the distribution within each dataset. Cells were marked as outliers and excluded if their mitochondrial gene content exceeded the threshold defined by three Median Absolute Deviations (MADs). Additionally, cells with a mitochondrial count percentage exceeding 10% were filtered out. A threshold of five MADs was also applied to the quality control covariates, including the total counts (`log1p_total_counts`), the cumulative percentage of counts for the top 20 expressed genes in a cell (`pct_counts_in_top_20_genes`) and the number of detected genes (`log1p_n_genes_by_counts`). SOLO,⁸⁷ a semi-supervised deep learning method, was used to identify and remove the potential doublets. We used the SOLO implementation from `scvi-tools` (v1.0.4)⁸⁶ and initialized SOLO with a pre-trained scVI model. The expression matrix underwent global scaling by normalizing gene expression measurements relative to the total expression per cell. Subsequently, the resulting values were scaled by a factor of 10,000 and natural logarithm transformation with a pseudocount value of 1.

Single-cell unsupervised clustering

For both human and murine data, clusters were identified using the Phenograph method,⁸⁸ which is a scalable graph-based clustering algorithm designed for high-dimensional single-cell data. We used the Phenograph-louvain algorithm integrated in scanpy. Batch correction was not performed to preserve the natural heterogeneity of lymphoma cells. Additionally, cells from the lymphoma tumor microenvironment such as T cells and LAMM cells were well-clustered without integration. For data visualization, high-dimensional single-cell data were reduced to two dimensions using the nonlinear dimensionality reduction algorithm UMAP (Uniform Manifold Approximation and Projection).⁸⁹ Additionally, signature LAMM score in scRNA-seq data was computed using `scanpy.tl.score_genes`.

Differential gene analysis

Analysis of differentially expressed genes was performed to identify marker genes specific to each cell cluster. These analyses involved comparing the gene expression profiles of each cluster against those of all other clusters, using the Wilcoxon rank-sum test on normalized gene expression data. To identify these marker genes, we utilized the FindMarkers function from the Seurat (v5.0.0) R package⁹⁰ which subsequently adjusts the resulting *p* values using Bonferroni correction to account for multiple testing. Genes were considered as differentially expressed if their adjusted *p* value was less than 0.05.

Cell-cell interactions

To identify cell-cell interactions, CellPhoneDB (v5)^{40,91} was used for predicting communication between cells. In essence, this involved inferring potential receptor-ligand interactions between a pair of clusters based on the expression of a receptor by one

cluster and a ligand by another. Genes expressed by fewer than 10% of the cells within a cluster were filtered out. For the murine data, we followed CellPhoneDB documentation and converted gene IDs to their corresponding human orthologues before conducting the interaction analysis. The R package *ktplots* (v2.4.2)⁹¹ was used to visualize the chord diagrams.

RNA velocity analysis

The *velocyto* R package (v0.17.17)⁹² was used to quantify spliced and unspliced UMIs for each gene in each cell. Subsequent analyses were performed using *scanpy* (v1.10.3) and *scvelo* (v0.3.3),⁹³ a scalable toolkit for RNA velocity analysis in single cells. Count matrices were normalized by library size, and the top 2000 highly variable genes were selected from those with at least 20 expressed counts in both spliced and unspliced mRNA. Principal component analysis (PCA) was then applied to the log-transformed spliced matrix, and the top 30 principal components were used to construct a k-nearest neighbor (k-NN) graph. For each cell, first- and second-order moments (means and uncentered variances) of normalized spliced and unspliced counts were computed based on its 30 nearest neighbors. These moments were then used for RNA velocity estimation in dynamical mode. Additionally, Partition-based Graph Abstraction (PAGA)⁹⁴ was applied to summarize information from RNA velocity.

Gene set enrichment analysis

We performed GSEA, utilizing pre-ranked GSEA, as implemented by the Python package *gseapy*,⁹⁵ to identify enriched gene pathways based on differentially expressed genes within the single-cell data. For the assessment of enriched pathways within T cell clusters, we leveraged a curated set of pathways sourced from MSigDB (C5, ontology gene sets).¹⁰⁹ We considered pathways with adjusted *p* values < 0.05 as statistically significant.

Pathway activity analysis

Mouse reference data for pathway activity inference were obtained from PROGENy (Pathway RespOnsive GENes for activity inference),¹¹⁰ a curated resource of fourteen signaling pathways and their target genes, complete with *p* values and interaction weights. In our analysis, pathway activity inference relies on the complete set of footprint genes for each pathway. To infer pathway activity scores at the single-cell level, we used the Python package *decoupler* (v1.9.2).⁹⁶

Single-cell gene expression analysis of the human LAMM cells

We compared the expression levels of LAMM-associated genes in LAMM cells from patients with NDR and DR. The difference between the two groups was assessed by calculating the fold change in mean gene expression between NDR and DR patients. Cells with zero counts for a given gene were excluded from the analysis before comparison.

Single-cell CAR-T_{reg} analysis from peripheral blood

Frequency of CSF1⁺ CAR-T cell populations and mean CSF1 expression levels were analyzed from previously published scRNA-seq data of CAR-T cells obtained from peripheral blood of axicabtagene ciloleucel-treated B-NHL patients at Stanford.⁹ Three out of nine samples passed quality control (CSF1: ≥ 25 cells within CAR-T_{reg} population) and were hence used for downstream analysis.

Flow cytometry

Flow cytometry was conducted to assess transduction efficiencies for both human and murine anti-CD19 CAR-T cells, identify murine anti-CD19 CAR-T cell expansion *in vivo*, determine cell viability after co-culture of lymphoma cells with human anti-CD19 CAR-T cells and characterize surface markers expressed on human monocytes and LAMMs, respectively. To this end, we used the following antibodies. For human anti-CD19 CAR-T cell detection: anti-CD3 APC (Miltenyi), anti-idiotypic CD19 CAR Biotin (Miltenyi) or anti-mouse IgG Fab Biotin (Southern Biotech) together with anti-Biotin PE (Miltenyi). For murine anti-CD19 CAR-T cell analysis: anti-rat IgG Fab Biotin (Jackson Immuno), Streptavidin-PE (BioLegend) and anti-mouse CD3 ϵ APC (BioLegend). For quantification of tumor cell viability and T cells after co-culture (Beckman Coulter Cytoflex LX Flow Cytometer or BD Symphony A3, respectively): anti-CD3 BV605 (BioLegend) or anti-CD3 APC (BioLegend), anti-CD20 AF700 (BioLegend) or anti-CD20 PE (BioLegend), anti-CD4 BV510 (BioLegend), anti-CD8 BUV737 (BD Bioscience), anti-CD27 PE/Cy7 (BioLegend), Zombie UV or NIR Viability dyes (BioLegend). To characterize human monocytes and LAMMs: anti-HLA-DR BUV737 (BD Bioscience), anti-CD16 BUV805 (BD Bioscience), anti-CD11b BV510 (BioLegend), anti-CD45 BV570 (BioLegend), anti-CD86 BV605 (BioLegend), anti-CD163 BV785 (BioLegend), anti-CD62L FITC (BioLegend), anti-CD68 PerCP/Cyanine 5.5 (BioLegend), anti-CD80 PE (BioLegend), anti-CD14 PE/Dazzle 594 (BioLegend), anti-PD-L1 PE/Cy7 (BioLegend), anti-CD15 APC (BioLegend), anti-CD33 Alexa700 (BioLegend) anti-CD206 APC/Fire750 (BioLegend), anti-CSF1R/CD115 BV421 (BioLegend). Samples were incubated for 5 min at room temperature with Fc receptor blocking solution (BioLegend). Afterwards, samples were stained with respective antibody mix, incubated for 30 min at 4°C followed by PBS washing prior to analysis. For secondary antibody stainings samples were incubated again for 30 min at 4°C and hereafter washed again with PBS. Samples were analyzed on the Beckman Coulter Cytoflex LX Flow Cytometer and the BD Symphony A3.

Multiplex analysis of cytokines

For multiplexed cytokine analysis, we used Luminex xMAP technology to quantitatively and simultaneously detect cytokines and chemokines. The multiplexing analysis was performed by Eve Technologies Corporation (Calgary, Alberta, Canada) using the

Luminex 200™ system (Luminex Corporation/DiaSorin, Saluggia, Italy) with Bio-Plex Manager™ software (Bio-Rad Laboratories Inc., Hercules, California, USA). The following panels were used: Human Cytokine/Chemokine Panel A 48-Plex Discovery Assay Array (HD48A) and the Eve Technologies' Human Cytokine Proinflammatory Focused 15-Plex Discovery Assay Array (HDF15) according to the manufacturer's protocol.

Immunohistochemistry

3 μm tissue sections of FFPE primary B-NHL specimens or diseased spleens of CAR-T cell treated mice were deparaffinized, placed in 200mL of target retrieval solution (EDTA buffer pH 9.0 or Citrat buffer pH 6.0, respectively) and heated for 20 min at boiling temperature. Afterwards, sections were washed with TBS. Immunohistochemical staining was performed using the LabVision Autostainer-480S (ThermoFisher) using the horseradish-peroxidase polymer method. Endogenous peroxidase activity was blocked by treatment with H₂O₂ for ten min. Staining was done using hematoxylin & eosin (H&E), primary antibodies and the Secondary-Histofine-Simple-Stain (SHSS) antibody detection kit (Medac). Human primary FFPE tissue sections were diagnosed based on routine histological examination including H&E and CD20 staining by trained hematopathologists and stained with a primary antibody against CSF1R (clone SP211) (Abcam). Mouse FFPE tissue sections were stained with a primary antibody against B220 (clone RA3-6B2) (BD Bioscience).

Quantification of immunohistochemical staining

CSF1R protein expression was quantified by using the semi-quantitative image analysis software QuPath (v0.50), as described earlier.⁹⁷ First, all slides were scanned and images digitalized with the Panoramic-250 slide scanner (3D Histech). After manually choosing the lymphoma areas the program was run on all region of interest (ROIs) quantifying immunopositive cells within the ROI. The frequency of CSF1R⁺ cells was calculated by H-Score. A minimum of 5000 (range: 5,516 - 202,095, median: 56,409) cells total per patient was analyzed.

Immunofluorescence of murine samples

For immunofluorescence staining of diseased spleens of CAR-T cell treated mice, 3 μm FFPE tissue sections were deparaffinized, placed in 200mL of target retrieval solution (Citrat buffer pH 6.0) and heated for 20 min at boiling temperature. Afterwards, sections were washed with TBS, followed by blocking with BSA 3%. The sections were then incubated with the following primary antibodies overnight at 4°C: anti-CD3 (clone SP7) (ThermoFisher) and rabbit anti-mouse anti-CSF1R AF647 (clone EPR23529-26) (Abcam). Sections were incubated with an anti-rabbit IgG secondary antibody AF568 (Abcam). DAPI staining was used to visualize nuclei, and slides were mounted with ProLong Gold Antifade Mountant (Invitrogen). Imaging and microscopic analyses were performed using a Stellaris 5 (Leica) microscope. Brightness and contrast were adjusted using Fiji (v1.54f) for visualization purposes.

IMC image acquisition of tissue microarrays

Representative ROIs from FFPE primary lymphoma specimens (human) or diseased spleens (murine) were selected by an experienced hematopathologist. For both, human and murine specimens, a tissue microarray (TMA) was generated with 1 or 2 cores of 1.5 mm diameter per sample using the Manual Tissue Arrayer MTA-1 (Estigen) (murine samples) and the TMA Master II (3D Histech) (human samples). Fresh-cut tissue sections of 3 μm were used for further steps. IMC was performed by a Hyperion Imaging System (Standard BioTools, SBT), following a modified manufacturer's protocol and as described previously.¹¹¹

For CSF1R staining of human lymphoma specimens we applied an amplification strategy using the Tyramide superboost kit (ThermoFisher) and 165Ho metalated DTPA-diTy. In brief, antigen retrieval (EDTA buffer pH 9.0) of FFPE tissue sections was followed by incubation with 3% H₂O₂ at room temperature and blocking with 10% goat serum. Then, the sections were labeled with a CSF1R antibody (clone SP211) (Abcam) diluted in 0.5% BSA and incubated for 20 min followed by incubation with an anti-rabbit immunoglobulin-HRP for 1 h at room temperature. Finally, the tyramide working solution including 165Ho metalated DTPA-diTy was applied to the section. This procedure was followed by IMC antibody staining. In brief, the slides were incubated with the antibody cocktail in a hydration chamber at 4°C overnight. DNA was stained by 1:800 500 μM Intercalator-Ir solution (SBT) in TBS for 30 min at room temperature in a hydration chamber. When possible, ROIs of 1 mm² (1000 μm × 1000 μm) were laser-ablated (frequency 200 Hz, laser power 3 a.u.).

IMC image preprocessing

For both human and mouse tissues IMC images were converted to .tiff files. Hot pixels were identified as pixels brighter than the local maximum (kernel of size (5,5)) by a factor equal to the 50th percentile of image pixel intensities. After detection the intensity of these hot pixels were capped to their local maximum. Images corresponding to marker channels of interest (Tables S2) were further manually inspected to exclude low quality or nonspecific staining. Marker expression was analyzed based on positive pixels in each image, as detected using a custom semi-automatic DBSCAN-based segmentation method.¹¹¹ First, pixels above the 99.9th percentile for each channel were clipped. The resulting pixel values for each image were normalized by dividing by the new maximum pixel value of that image. The DBSCAN (Density-based spatial clustering of applications with noise)¹¹² algorithm was applied to the pixel x-y coordinates, using the previously generated corresponding pixel values as sample weights. Only pixels with non-zero weights are input to DBSCAN. DBSCAN is clustering the pixels into as many clusters as necessary, generating connected components that we consider as foreground pixels. On the connected components with an area larger than 25 pixels, morphological operations were applied:

dilation with a disk of radius 5, erosion with a square matrix of dimension 3 filled with 1s, followed by closing with a disk of radius 2. Several parameters were tested for the DBSCAN algorithm: epsilon in [1, 2, 3, 5] and minimum samples in [1, 2, 5], while leaf_size=5, metric='manhattan' were kept constant (scikit-learn implementation). After manual inspection, one value pair for epsilon and minimum samples was chosen for all images of one slide for one channel. The pixel percentages, corresponding to the foreground pixels detected via this DBSCAN-based segmentation (pixel percentage = pixel sum / image size), were used for downstream analysis.

Downstream analysis of human IMC data

Pixels corresponding to the tissue were detected on a normalized sum of all channel images. Marker expression of CD3, CD8A and the union of CD14 and CD68, was defined as the percentage of positive pixels detected by the DBSCAN-based segmentation, relative to the tissue size (pixel percentage = pixel sum / area of tissue). In patients with two or more available ROIs, the percentage of pixels relative to the tissue was averaged.

Downstream analysis of murine IMC data

The murine IMC images of the corresponding channels (CD4, CD8 or CD11b) were first blurred using a Gaussian filter with a size of 20. A k-means algorithm (k = 3) was applied to the list of pixel values for each channel and only the class with the highest mean pixel value was considered as foreground. The edges of the foreground connected components were detected using a Canny filter with thresholds 100 and 200. Connected components with an area smaller than 1000 pixels, as well as connected components inside one another, were discarded. The intersections of enriched regions in CD4, CD8 and CD11b images were considered for the quantification of marker expression (Figures S7A–S7C). The marker expression were defined as the pixel percentages of CD3, CD4, CD8, CD11b, F4/80 and B220, respectively, based on each channel using the DBSCAN-based segmentation.

IMC distance analysis

Murine LAMM-positive regions were defined as the union of CD11b and F4/80 pixels and T cell-positive regions were defined based on the CD3 signal using DBSCAN-based segmentation described above. For each LAMM-positive region, we calculated the distance to the nearest T cell-positive region. Distances are defined between centroids of positive regions using the euclidean distance metric.

Tissue processing for MICS

Frozen embedded tissue specimens were cryosectioned with a CM3050 cryostat (Leica), 4 μm sections were mounted on SuperFrost Plus slides (Menzel). The cryosectioned slices on slides were directly stored at -80°C. On the day of use, the frozen slide was put in a 4% PFA solution and incubated for 10 min at room temperature. The slide was washed three times with MACSima Running Buffer (Miltenyi). Immediately after washing, a MACSwell Imaging Frame 4 (Miltenyi) was mounted on the slide and MACSima Running Buffer (Miltenyi) was added (according to the MACSwell Imaging Frames data sheet). Right before the start on the MACSima Instrument, a DAPI pre-staining was performed: The MACSima Running Buffer (Miltenyi) was removed and the sample was stained for 10 min with a DAPI staining solution. Finally, the DAPI staining solution was removed, three washing steps were performed and the initial sample volume of MACSima Running Buffer (Miltenyi) was added. Cyclic staining with 57 antibodies coupled to either FITC, PE or APC was done according to the manufacturer's instructions.

MICS image analysis

Image datasets (stack of images) were imported into the MACS iQ View Software (v1.3.1) (Miltenyi). The software uses nuclei and cell membrane markers to perform image segmentation identifying individual cells. After segmentation features like mean fluorescent intensities (MFI) were computed for each cell against the background and z-score normalized for visualization and comparability. Fluorescence overlays were assessed visually to capture spatial distribution of relevant cell types. In addition, unsupervised agglomerative hierarchical clustering into 30 clusters was performed and the resulting clusters annotated based on a heat map displaying antibody expressions in a given cluster. Clusters containing cells of the lymphoma tumor microenvironment like CAR-T cells, T cells and myeloid cells were further subclustered as needed and submitted to dimension reduction as UMAP by the MACS iQ analysis software.

QUANTIFICATION AND STATISTICAL ANALYSIS

Data processing and data analyses were performed using R, Python, Microsoft Excel, SPSS (IBM) and GraphPad Prism. Statistical tests were conducted using SPSS (IBM), R as well as GraphPad Prism and are indicated in the respective figure legend. *p* values below 0.05 were considered statistically significant and are indicated in the figures as follows: **p* < 0.05, ***p* < 0.01, ****p* < 0.001 and *****p* < 0.0001. We used FlowJo (FlowJo LLC) to analyze .fcs files derived from flow cytometry experiments. scRNA-seq analysis was performed in both R and Python. The code for IMC data analysis was written in python using as main packages scikit-image, numpy, scipy.ndimage, scikit-learn (for DBSCAN and k-means), and open-cv (Canny filter). Schematic illustrations in the Graphical Abstract and Figures 1A, 2E, 3A, 3K, 4O, and 5A were created using BioRender.